



Molecular docking and dynamic simulations of quinoxaline 1,4-di-*N*-oxide as inhibitors for targets from *Trypanosoma cruzi*, *Trichomonas vaginalis*, and *Fasciola hepatica*

Alonzo González-González¹ · Domingo Méndez-Álvarez¹ · Lenci K. Vázquez-Jiménez¹ · Timoteo Delgado-Maldonado¹ · Eyra Ortiz-Pérez¹ · Alma D. Paz-González¹ · Debasish Bandyopadhyay² · Gildardo Rivera¹

Received: 25 December 2022 / Accepted: 2 May 2023 / Published online: 17 May 2023
© The Author(s), under exclusive licence to Springer-Verlag GmbH Germany, part of Springer Nature 2023

Abstract

Context Quinoxaline 1,4-di-*N*-oxide is a scaffold with a wide array of biological activities, particularly its use to develop new antiparasitic agents. Recently, these compounds have been described as trypanothione reductase (TR), triosephosphate isomerase (TIM), and cathepsin-L (CatL) inhibitors from *Trypanosoma cruzi*, *Trichomonas vaginalis*, and *Fasciola hepatica*, respectively.

Methods Therefore, the main objective of this work was to analyze quinoxaline 1,4-di-*N*-oxide derivatives of two databases (ZINC15 and PubChem) and literature by molecular docking, dynamic simulation and complemented by MMPBSA, and contact analysis of molecular dynamics' trajectory on the active site of the enzymes to know their potential effect inhibitory. Interestingly, compounds Lit_C777 and Zn_C38 show preference as potential *Tc*TR inhibitors over *Hs*GR, with favorable energy contributions from residues including Pro398 and Leu399 from Z-site, Glu467 from γ -Glu site, and His461, part of the catalytic triad. Compound Lit_C208 shows potential selective inhibition against *Tv*TIM over *Hs*TIM, with favorable energy contributions toward *Tv*TIM catalytic dyad, but away from *Hs*TIM catalytic dyad. Compound Lit_C388 was most stable in *Fh*CatL with a higher calculated binding energy by MMPBSA analysis than *Hs*CatL, though not interacting with catalytic dyad, holding favorable energy contribution from residues oriented at *Fh*CatL catalytic dyad. Therefore, these kinds of compounds are good candidates to continue researching and confirming their activity through in vitro studies as new selective antiparasitic agents.

Keywords Quinoxaline 1,4-di-*N*-oxide · Trypanothione reductase · Triosephosphate isomerase · Cathepsin-L · *Trypanosoma cruzi* · *Trichomonas vaginalis* · *Fasciola hepatica*

Introduction

Currently, in silico studies in drug design and development have allowed to obtain new and improved treatments for various diseases. Ligand-based and structure-based virtual screenings are strategies to find new molecules as specific

inhibitors from available chemical libraries [1, 2]. The use of chemical scaffolds presents an opportunity to carry out ligand-based virtual screening (LBVS) assays aimed at various biological targets reducing time and costs, although the validation of the biological effects is necessary in in vitro models.

The quinoxaline ring is a versatile scaffold in medicinal chemistry to obtain new candidate drugs. These compounds have many biological effects including antibacterial, antiprotozoal, and anticancer activity. Quinoxaline 1,4-di-*N*-oxide (QNO) is a highlight for its trypanocidal, trichomonacidal, and antihelminthic activity [3–8]. In this sense, recently, QNO derivatives have been reported as inhibitors (Fig. 1a–c) of *Trypanosoma cruzi* trypanothione reductase (*Tc*TR), which plays a central role in the trypanothione dependent

✉ Gildardo Rivera
gildardors@hotmail.com

¹ Laboratorio de Biotecnología Farmacéutica, Centro de Biotecnología Genómica, Instituto Politécnico Nacional, 88710 Reynosa, México

² Department of Chemistry and SEEMS, University of Texas Rio Grande Valley, Edinburg, TX 78539, USA

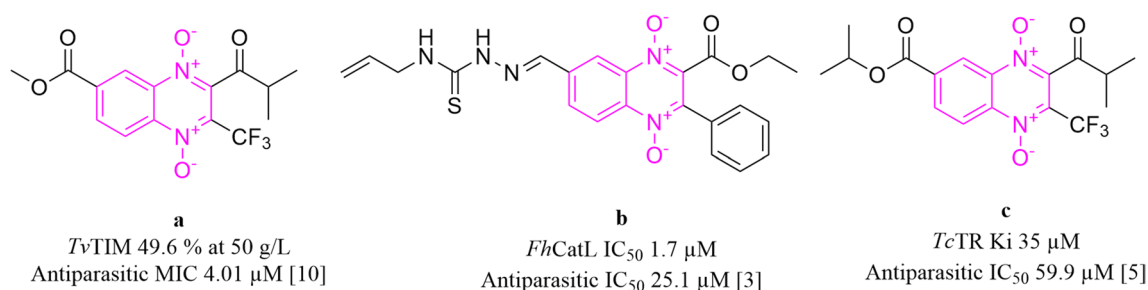


Fig. 1 Quinoxaline 1,4-di-*N*-oxide derivatives are inhibitors of *Tc*TR, *Tv*TIM, and *Fh*CatL and antiparasitic agents

redox system of the trypanosomatid [4, 5, 9], *Trichomonas vaginalis* triose phosphate isomerase (*Tv*TIM), which is central in the glycolytic pathway mediating the conversion of triosephosphates [10–13], and *Fasciola hepatica* cathepsin L (*Fh*CatL), which has been reported to be needed by the nematode for their nutritional supply as well as enhancing evasiveness into host tissue [3, 14, 15]. Therefore, in this study, the objective was to analyze the affinity of QNO derivatives reported on the active site of *Tv*TIM, *Fh*CatL, and *Tc*TR by molecular docking and molecular dynamics simulations to know their potential inhibitory effect.

Additionally, the potential selectivity was determined using the human counterpart glutathione reductase (*Hs*GR), triose phosphate isomerase (*Hs*TIM), and cathepsin-L, (*Hs*CatL) for *Tc*TR, *Tv*TIM, and *Fh*CatL, respectively.

Methodology

Protein preparation

Crystal structures of *Tc*TR, *Hs*GR, *Tv*TIM, *Hs*TIM, *Fh*CatL, and *Hs*CatL were obtained from the database Protein Data Bank (PDB) with access codes 1BZL, 4GR1, 3QST, 4POC, 2O6X, and 6EZX, respectively. All crystal structures were prepared using open access software UCSF-Chimera 1.13 [16], removing all co-crystallized molecules and utilizing the built-in tool Dock Prep to add hydrogens and charges to protein crystals.

Ligand library preparation

Ligands were obtained from three different sources: chemical databases ZINC15 and PubChem, and 43 journal articles reported in PubMed (1970–2017). Ligand structures were searched on both chemical databases utilizing the built-in search tool, limiting the search to *substructure*. All reports found in the PubMed database studying QNO were used to gather chemical structures; these were drawn in open access software MarvinSketch (ChemAxon) for further use. All structures were filtered out considering Lipinski's rules as

inclusion criteria for selected compounds. The three structure libraries were energy minimized and converted to .mol2 format utilizing open access Open Babel 3.1 software [17].

Molecular docking

MGL Tools 1.5.6 software was used to convert all protein crystals and ligands to the .pdbqt format required to conduct molecular docking simulations [18]. AutoDock Vina software 1.1.2 was used to perform molecular docking simulations for all ligands [19]. Simulations were done considering a cubic grid box with edge and length of 24 Å. For *Tc*TR, *Hs*GR, *Tv*TIM, and *Hs*TIM, a grid box was centered on the active site of the protein crystals, as it is reported to be preferred binding site for QNO derivatives [4, 5, 20, 21]. In the case of *Fh*CatL, blind docking was carried out to determine the most favorable docking site for the QNO derivatives, to be later used in site-directed docking, *Hs*CatL crystal was 3D aligned with *Fh*CatL with USCF-Chimera software, and coordinates were shared for site-directed docking. Coordinates for the grid box center for site-directed docking are summarized in Table 1.

Docking analyses

The docking simulations' results were analyzed following two criteria: binding free energy (FEB) and interaction analyses with amino acid residues.

Table 1 Coordinates for grid box center for site-directed docking simulations for all protein crystals

Crystal	X	Y	Z
<i>Tc</i> TR	65.805	5.055	0.955
<i>Hs</i> GR			
<i>Tv</i> TIM	−8.704	31.659	−14.097
<i>Hs</i> TIM	17.667	−17.812	12.563
<i>Fh</i> CatL	26.590	21.701	13.613
<i>Hs</i> CatL			

Free energy of binding analysis

The FEB values of the QNO derivatives were used sequentially in two manners to select which compounds to consider for further testing. First, the FEB of the tested ligand was compared with the FEB of the natural ligand of each protein; this was regarded as a first inclusion criterion; compounds with a lower FEB than the natural ligand were considered for further analysis, and this comparison followed results of Eq. 1. Second, the FEB of the tested ligands were contrasted between the value obtained for the parasite protein versus the human homolog: for *T. cruzi* analysis, the value obtained for *TcTR* was compared to *HsGR*; in the case of *T. vaginalis*, the value obtained for *TvTIM* was compared to the value obtained for *HsTIM*, as for *F. hepatica* it was compared with human homolog *HsCatL*; these analyses followed the results of Eq. 2.

$$\Delta_1 = \text{FEB}_{\text{NL}} - \text{FEB}_{\text{QX}}$$

Equation 1 shows the comparison of binding affinity between tested QNO structure and natural ligand, inclusion of compounds with a higher affinity for the active site than natural ligand: FEB_{NL} is free energy of binding of natural ligand, the FEB_{QX} is free energy of binding of QNO, if $\Delta_1 \geq 0$, QNO is included, and if $\Delta_1 < 0$, QNO is excluded.

$$\Delta_1 = \text{FEB}_{\text{Hs}} - \text{FEB}_{\text{Tc/Tv}}$$

Equation 2 shows the comparison of QNO on each of the receptors to determine their specificity toward human homolog versus parasite protein, inclusion of compounds with a higher affinity toward parasite protein: FEB_{Hs} is free energy of binding for QNO on human homolog, $\text{FEB}_{\text{Tc/Tv}}$, free energy of binding for QNO on parasite protein, if $\Delta_2 \geq 0$, QNO is included, and if $\Delta_2 < 0$, quinoxaline is excluded.

The compounds that complied with both inclusion criteria were further analyzed. By considering both criteria as equally important, these were evaluated in accordance with Eq. 3, geometrical distance, where each delta calculated may be represented by two perpendicular axes and their compound magnitude calculated as presented below as a geometrical distance.

$$\text{geometrical distance} = \sqrt{(\Delta_1)^2 + (\Delta_2)^2}$$

Equation 3 shows the geometrical distance, measuring compound magnitude of affinity toward parasite protein by considering Δ_1 and Δ_2 .

The FEB values for *FhCatL* were used to order the ligands from the most active to the least active without any other analyses. The top 10 compounds according to geometrical distance were analyzed to determine the interactions present in the receptor-ligand complex obtained by molecular docking analysis. The interactions were determined using an online server Protein–Ligand Interaction Profiler (PLIP)

[22]. The interaction profiles for the tested compounds were compared to the interactions observed for natural ligand and known inhibitors.

Filtering of top scored compounds for molecular dynamics

To have a reduced library of candidates for molecular dynamics, interaction profiles for top scored compounds were compared with those obtained for the natural ligand and known inhibitors. Derivatives with the most hydrogen bonding interaction with residues shared with natural ligand or known inhibitor were considered for further analysis. Within this reduced group, the compounds were clustered considering structural similarity using Tanimoto coefficient to generate distance trees, considering one compound from each distinct branch for further testing. Finally, a visual inspection was considered to assure that no compound is redundant in two libraries.

Molecular dynamic analysis

Molecular dynamic analysis was performed with GROMACS version 2018.4 [23] employing the AMBER03 force field [24]. First, the topology of each compound selected by LBVS was generated with ACPYPE Antechamber module [25] with the General Amber Force Field [26]. The solvation was done with water molecules in a dodecahedron with a minimum distance from the wall of 10 Å, using the TIP3P water model [27]. Then, sodium and chloride ions were added to neutralize the system with an energy minimization of 50,000 times. The system was energy-minimized by the steepest descent algorithm. Then, two equilibrium steps were performed at 300 K. First, the compound was simulated at NVT conditions (constant number of particles, volume, and temperature) using a V-rescale thermostat [28] considering a time constant (τ_t) of 0.1 ps obtaining velocities according to Maxwell–Boltzmann distribution. For the second step, the compound was simulated at NPT conditions (constant number of particles, pressure, and temperature) utilizing a V-rescale thermostat and a Berendsen barostat [29] with time constants (τ_t and τ_p) of 0.1 and 2.0 ps, respectively. Each stage achieved a duration of 100 ps. Finally, the simulation was performed at a temperature of 300 K for a trajectory of 120 ns using V-rescale thermostat and Parrinello–Rahman barostat [30] with τ_t and τ_p of 0.1 and 2.0 ps, respectively [31, 32]. The calculation to the long-range electrostatic interactions was done using the Particle Mesh Ewald method [33], and the LINCS algorithm was used for the H-bond length constrains [34]. The root mean square deviation (RMSD), root mean square fluctuation (RMSF), and radius of gyration (gyr) of each complex were obtained to determine the stability of the complex. Additionally, to understand the interaction behavior

observed during the dynamics' trajectories, H-bond count and contact analysis were carried out. Contact analysis was done for the last 4000 frames (one frame every 10 ps for the 80 to 120 ns portion of the dynamics' trajectory) using ProLIF software version 1.1.0 [35]; H-bond counting was done with built-in GROMACS *hbond* function.

MMPBSA analysis

The binding energies and per-residue decomposition were carried out with *g_mmpbsa* version 5.1.2 [36, 37]. For this analysis, most stable compounds analyzed by molecular dynamics on each of the tested proteins were considered. A total of 200 frames from 80 to 120 ns were evaluated with an extraction of every 200 ps of the protein–ligand complex trajectory. The calculation of the non-polar solvation energy was done with the solvent accessible surface area (SASA) model. The energy contribution of each residue of each of the proteins in the binding to the ligand was recovered with *MmPbSaDecomp.py* for which the heatmap was prepared considering a cut-off energy score of 0.9 kcal/mol which is equivalent to a weak hydrogen bond interaction [38].

Results and discussion

A total of 1851 molecules with the QNO scaffold were docked on the active site of *TcTR*, *HsGR*, *TvTIM*, *HsTIM*, *FhCatL*, and *HsCatL*: 801 from journal articles, 121 from ZINC15 database, and 929 from PubChem database. These were then included or excluded in accordance with Eqs. 1 and 2 to obtain those compounds predicted to interact favorably with parasite protein better than natural ligand and with higher affinity for parasite protein than human homolog.

QNO derivatives on *TcTR-HsGR*

TcTR-HsGR FEB analysis

From the QNO libraries docked in *TcTR-HsGR*, the number of ligands that had a higher affinity than trypanothione disulfide (FEB 8.8 kcal/mol) were as follows: literature (65/801), ZINC15 (12/121), and PubChem (28/929). Considering this new total, ligands which displayed a higher affinity toward parasite protein over human protein were as follows: literature (47/65), ZINC15 (10/12), and PubChem (28/28).

The top 10 compounds (Supplementary material) from each library were filtered considering interaction profile similarity to the natural ligand and/or known inhibitor profiles and then clustered by structural similarity using the Tanimoto coefficient to prepare distance trees, to then

choose from each branch representative compounds to include in molecular dynamic analysis. This filtering process reduced the candidate library considerably; at most, four compounds were obtained from each library following this methodology. To homogenize compound selection amount, top four compounds from each library are presented as final selection figures for each protein including compounds selected for molecular dynamics (bolded identifier). Figure 3 displays chosen representative compounds from each library docked on the active site of the *TcTR-HsGR*.

Common characteristics present in derivatives with a high affinity toward *TcTR* are the presence of large aromatic, heterocyclic, and aliphatic rings at 2- and 3- positions of the quinoxaline ring, similarly, halogenation, or halogenated substituents at 6- and 7- positions, nitrogen containing heterocycles, and protonable amines in flexible chains, being these latter mentioned characteristics reported as groups that favor biological activity thus supporting these findings [39].

TcTR-HsGR interaction analysis

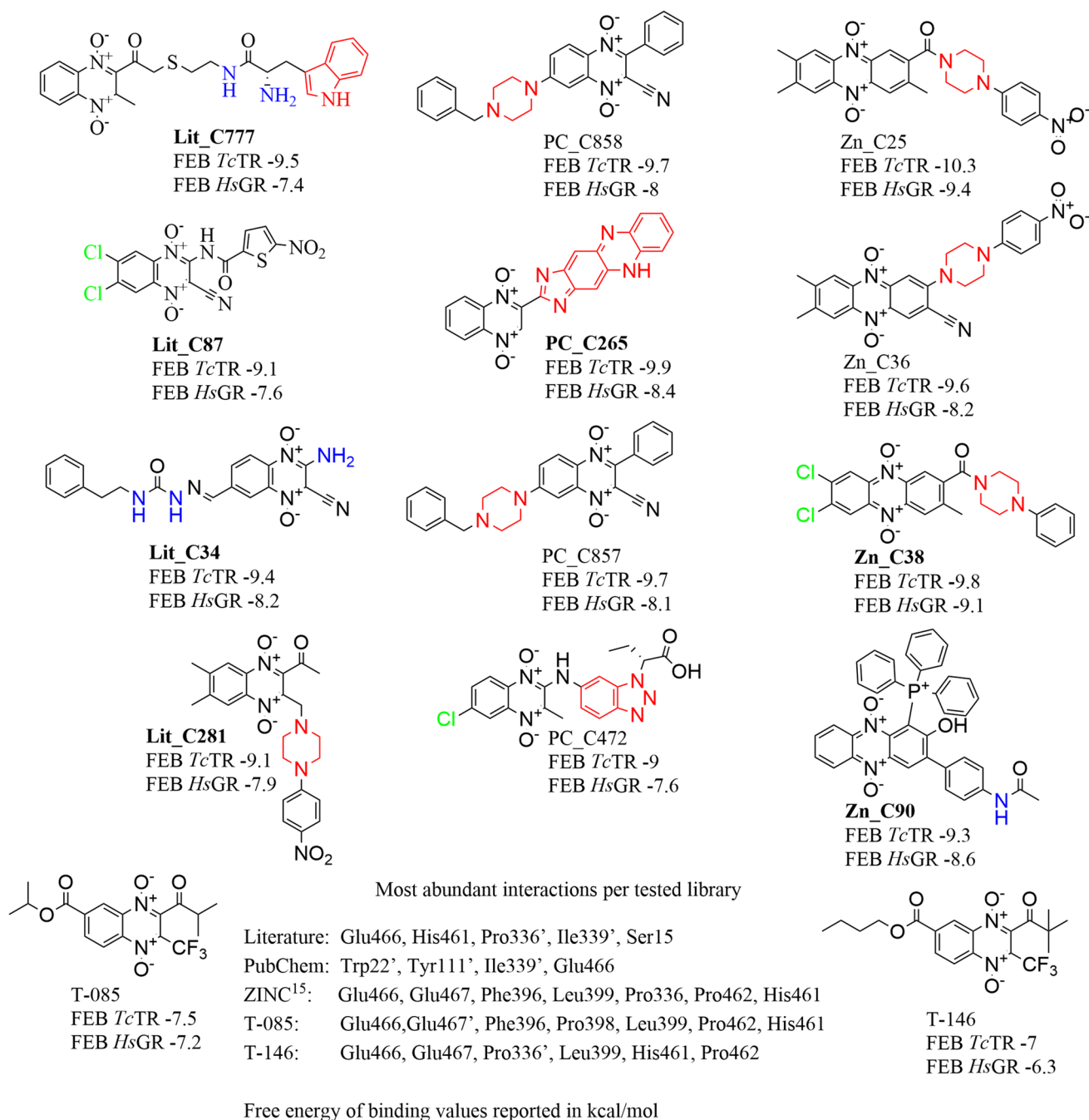
Upon the analysis of the interactions observed by the QNO structures with the highest FEB from each of the three sources, it was found that most of them were shared among them. A compilation of the observed interactions is presented in Fig. 2.

The interactions observed were predicted to be with amino acid residues reported as important for the binding of the natural ligand and trypanothione disulfide. In notable interactions with His461, one of three residues involved in catalysis. The interaction with residues Phe396, Pro398, and Leu399 is reported to be part of a subsite denominated Z-site part of the binding residues for natural ligand located within the interphase active site. Similarly, interactions with the hydrophobic cleft include Trp22 and Tyr111. As such these compounds derived from QNO can potentially inhibit the activity of trypanothione reductase by blocking the binding space needed by the natural ligand trypanothione disulfide. Any further design may consider these findings to enhance the activity of compounds. Figure 3 shows 3D representations of protein–ligand interactions for a representative compound from each library.

QNO derivatives on *TvTIM-HsTIM*

TvTIM-HsTIM FEB analysis

From the screening of QNO chemical libraries on *TvTIM* and *HsTIM* and docked scores for natural ligands found



Free energy of binding values reported in kcal/mol

Fig. 2 Top quinoxaline-1,4-di-*N*-oxide derivatives from each library with the highest binding affinity and the highest number of interactions of interest for *TcTR*; bold identifiers represent the compounds chosen for molecular dynamics testing

to be -4.6 and -4.8 kcal/mol for dihydroxyacetone phosphate and D-glyceraldehyde-3-phosphate, respectively, a selection was performed based on the FEB score. All tested ligands were shown to have a higher affinity than both natural ligands. Subsequent analysis showed that 651/801, 76/121, and 627/929 ligands from literature, ZINC15, and PubChem, respectively, had a higher affinity toward parasite over human enzyme.

Many of these ligands show a higher affinity even in comparison to the inhibitor reported by Vique-Sanchez et al. 2020 [12] (FEB -4.2 kcal/mol) and previously reported quinoxaline derivative EQX-NO 20 (-6.3 kcal/mol) [10]. Similarly, it may be observed that most compounds showed a higher affinity toward parasite versus human TIM homolog, which suggests that this type of compound has a high potential for parasite selective inhibition.

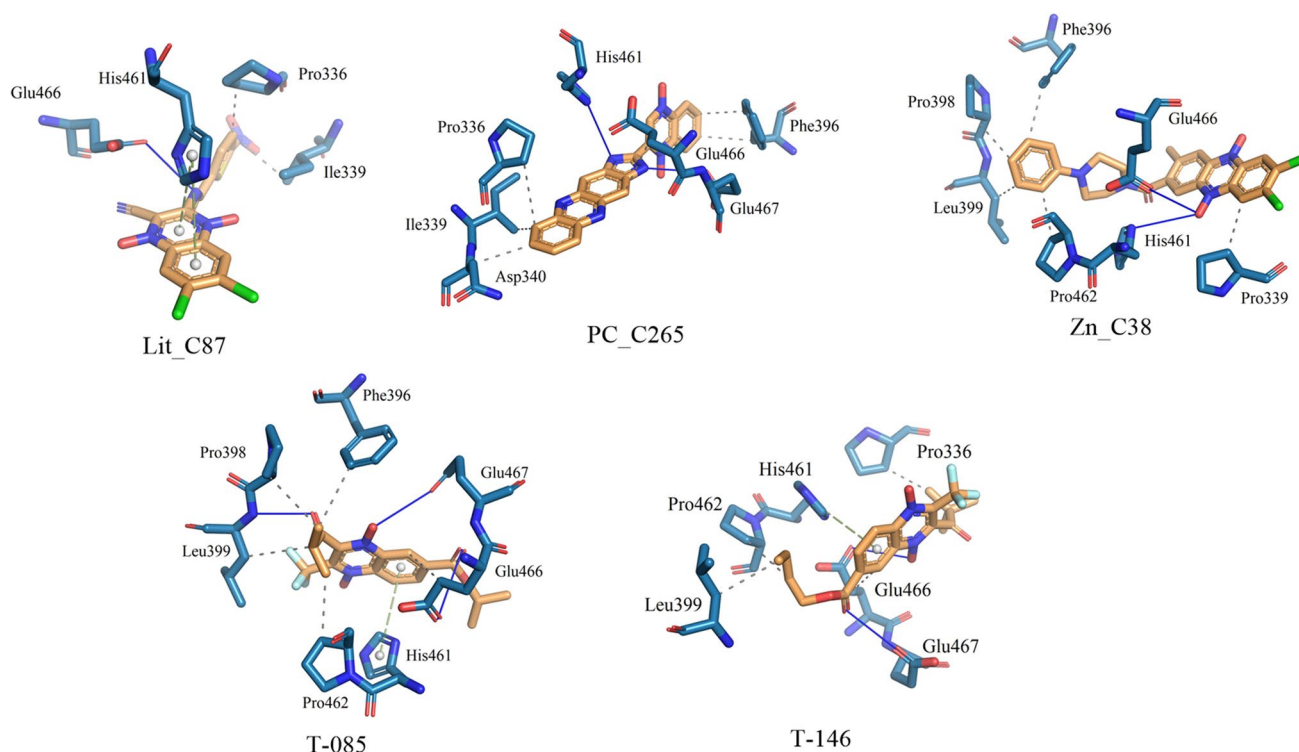


Fig. 3 Representative interactions with *TcTR* for the libraries analyzed by molecular docking: top left literature, top right PubChem, and bottom ZINC15: dotted black line hydrophobic interaction, solid blue line hydrogen bond, and dotted green line π -stacking interaction

Like for *TcTR/HsGR* analysis, a filtering methodology was applied to the top 10 scored compounds, to reduce the candidate library toward molecular dynamic analysis. Figure 4 displays chosen representative compounds from each library docked on the active site of the *TvTIM-HsTIM*.

This molecular docking analysis provided insight into the nature of promising substituents for the inhibition of *TvTIM*: large aromatic and halogenated substituents as well as carbonyl containing substituents which may favor affinity toward TIM protein.

The structural characteristics observed for compounds predicted to have a high affinity toward the binding to *TvTIM* were observed to be substitution with bulky groups, both aliphatic and aromatic, as well as nitrogen containing substituents at 2- and 3- positions, similarly, halogenation or halogenated groups and ester substituents at 6- and 7- positions. The presence of carbonyl substituents was observed in high scoring compounds, a characteristic which is consistent with mimicking natural ligand, as both substrates bear carbonyl groups.

TvTIM-HsTIM interaction analysis

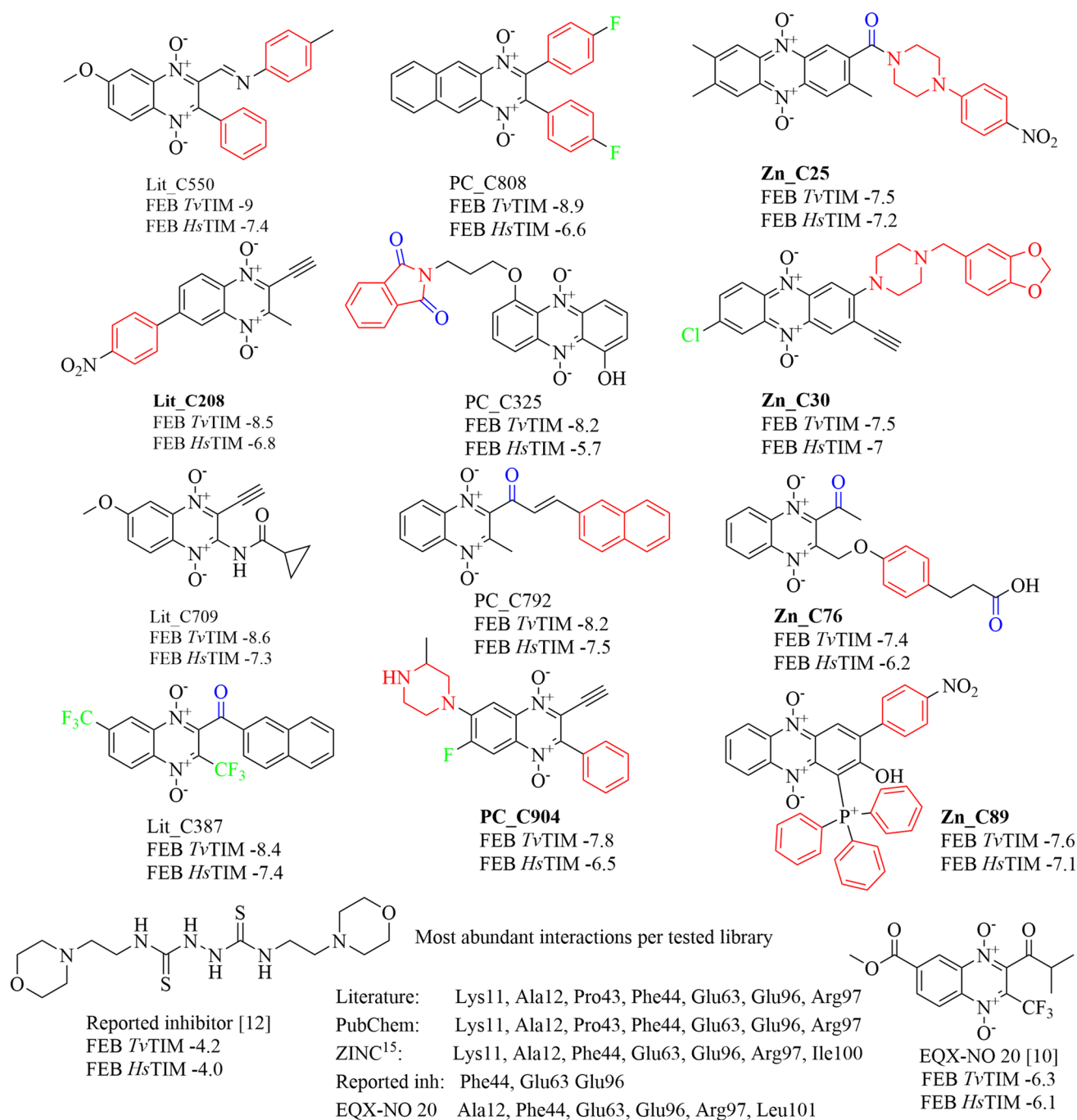
Analysis of the interactions of top scored QNO derivatives from the three tested libraries shows most derivatives interact with the identical residues: Lys11 (63%), Ala12 (63%), Pro43 (63%),

Phe44 (50%), Glu63 (77%), Glu96 (66%), and Arg97 (77%), for the first two mainly hydrophobic, Pro43 all hydrophobic, Phe44 half hydrophobic, and half hydrogen bond, for the last three primarily hydrogen bonding interactions. Interactions for Vique-Sánchez reported inhibitor: hydrogen bond: Phe44, Glu63, and salt bridge with Glu96, which are shared by most tested derivatives. These results coincide with the results already published by Vique-Sánchez et al. (2020), as well as the report by Benitez-Cardoza et al. (2021), where both observed that the most common interaction seen was with Lys11, Ala12, and Gly234 [11, 12] being the catalytic residues Lys13 and His95, here Lys11 and His94, and catalytic importance of residue Glu97, here Glu96 [40]. In this study, no interaction was seen with Gly234, but interactions with the other two residues are present for most derivatives. Representative interactions for QNO derivatives on *TvTIM* for each library are shown in Fig. 5, wherein all models, Glu63, Glu96, and Arg97 interact through hydrophobic and hydrogen bond interactions with the large hydrophobic cyclic substituents.

QNO derivatives on *FhCatL-HsCatL*

FhCatL-HsCatL FEB analysis

Molecular docking was carried out on the site found by blind docking strategy (Fig. 6). Figure 7 displays top-scored



Free energy of binding values expressed in kcal/mol

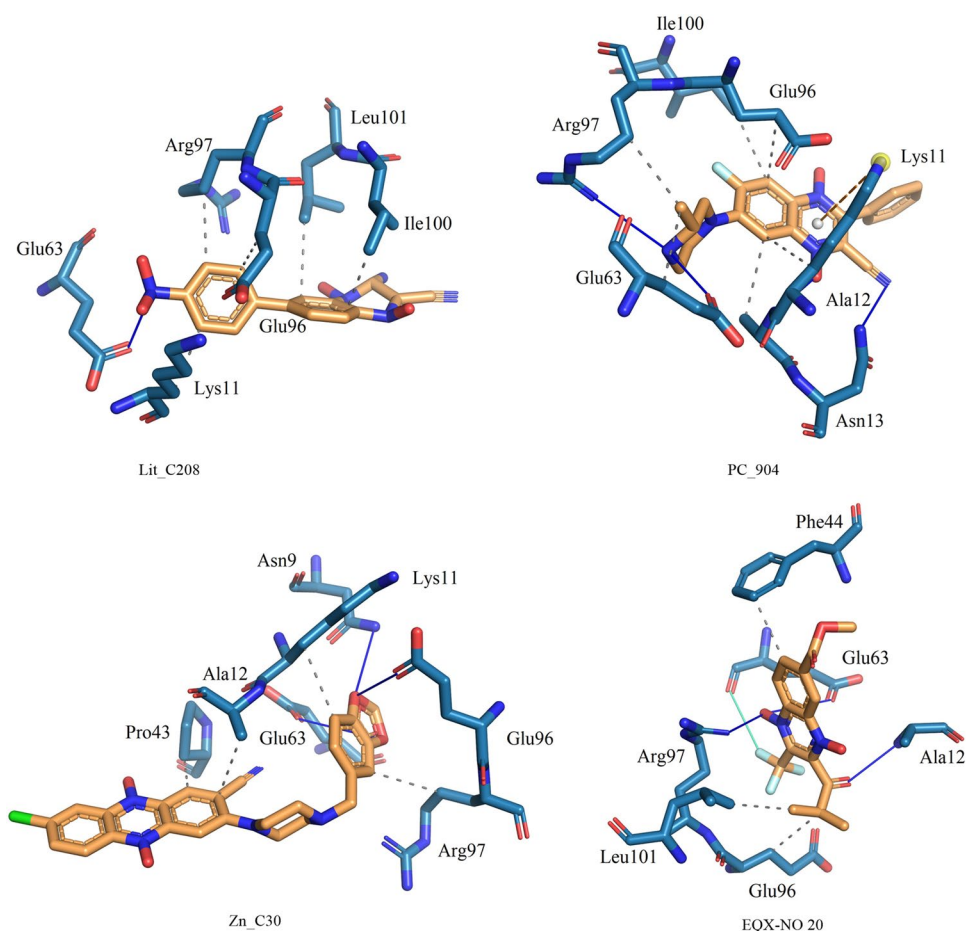
Fig. 4 Top quinoxaline-1,4-di-*N*-oxide derivatives from each library with the highest binding affinity and the highest number of interactions of interest for *TvTIM*; bold identifiers represent the compounds chosen for molecular dynamic testing

compounds from each library based on the FEB values toward *FhCatL*. Compounds C34 and C17 with FEB (−8.6 kcal/mol) were used as controls (known inhibitors). These were reported by Ferrara et al. (2016), the latter being a direct derivative of QNO and the former being the top

evaluated compound for Ferrara's research group. Tables listing the top 10 compounds for each library can be found in supplementary materials.

The common characteristics present in derivatives with the most affinity toward *FhCatL* are bulky groups, aliphatic,

Fig. 5 Representative interactions with triosephosphate isomerase for the libraries analyzed by molecular docking: top left literature, top right PubChem, and bottom ZINC15: dotted black line hydrophobic interaction, solid blue line hydrogen bond, dotted orange line π -cation interaction, and solid cyan line halogen interaction



aromatic, and heterocyclic, halogenated substituents, and protonable amines, in both the open chain and cyclic secondary amines. As it may be observed, most characteristics are hydrophobic; still, there is a presence of polar substituents such as protonable amine, nitro, and hydroxyl groups which suggest that the binding site can interact with both hydrophobic and hydrophilic substituents, which is congruent with a protease which may need to interact with both simultaneously.

FhCatL interaction analysis

Analysis of the interactions of top scored QNO derivatives from the three tested libraries shows most derivatives interact with the identical residues: Val47 (67%), Tyr49 (77%), Glu230 (77%), Asp232 (73%), and Gln244 (83%), for the first three mainly hydrophobic interactions, for Asp232 and Glu244, about half hydrophobic half hydrogen bond interactions. Three of these five predominant interactions observed for QNO derivatives are shared with the binding poses of two reported inhibitors C17 and C34 at the site determined by blind docking: Val47, Asp232, and Gln244. As this study was carried out on the site determined by blind docking

(Fig. 6), there is no direct comparison with previous studies. Still, it is noteworthy that most interactions were shared among the different chemical libraries tested, emphasizing

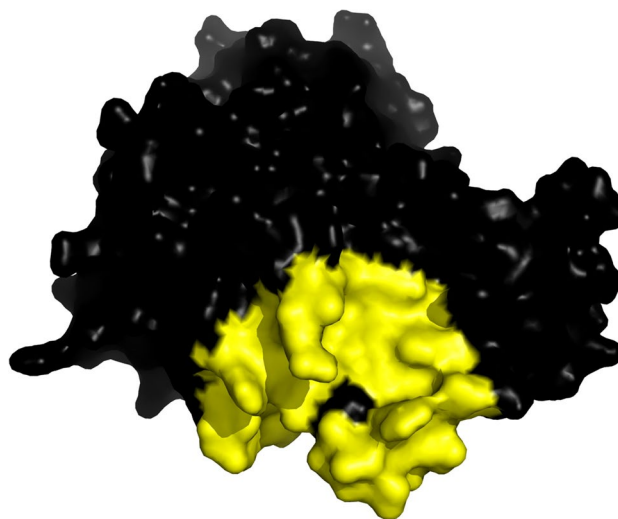


Fig. 6 The docking site on *FhCatL* was found by blind docking of a sample series of QNO derivatives and used for further site-directed docking studies of all tested quinoxaline derivatives

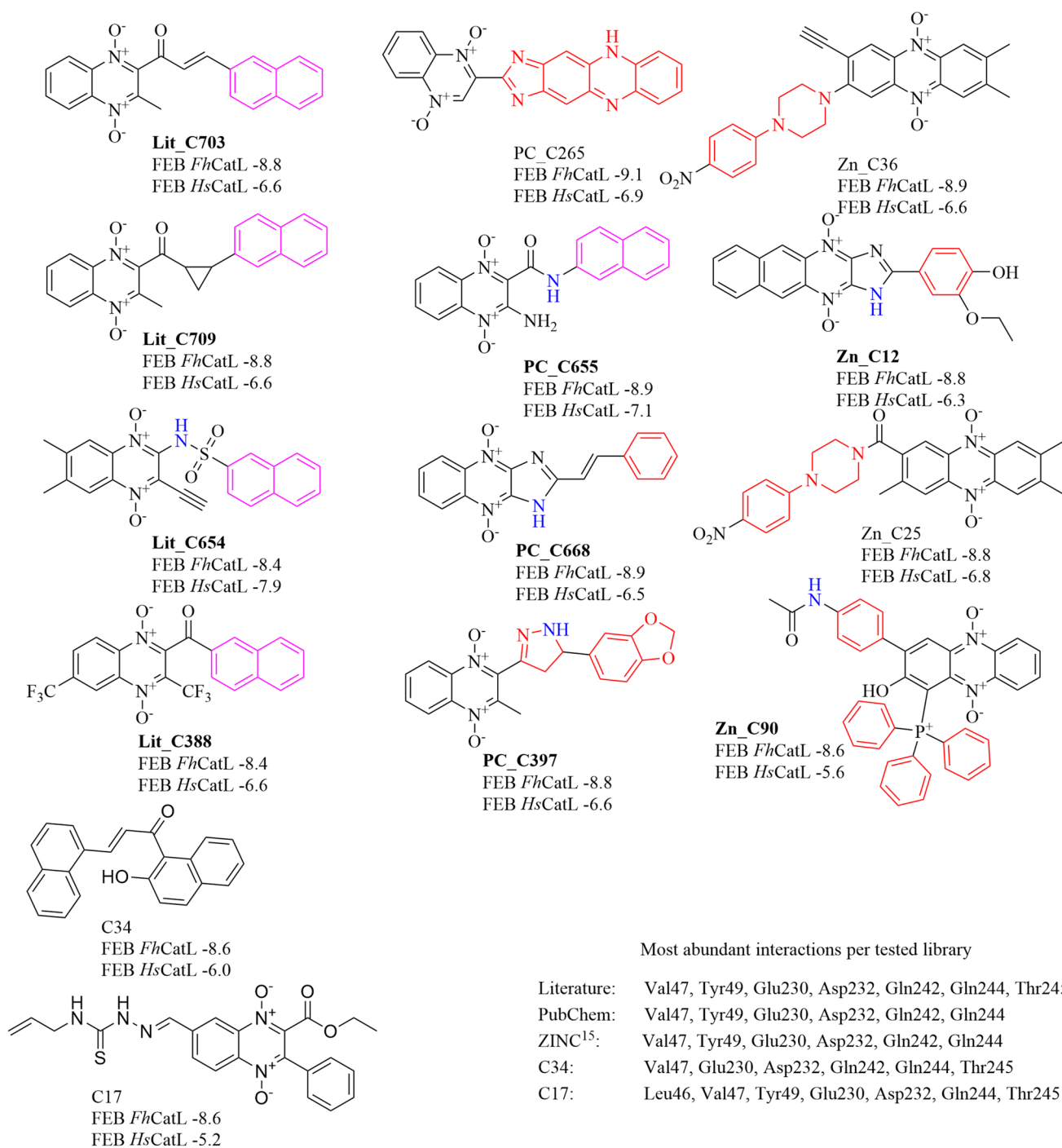


Fig. 7 Top quinoxaline-1,4-di-*N*-oxide derivatives from each library with the highest binding affinity and the highest number of interactions of interest for *FhCatL*; bold identifiers represent the compounds chosen for molecular dynamics testing

the preference that these types of derivatives have with the found site. A compilation of the observed interactions is presented in Fig. 7. Representative interaction visual representation may be observed in Fig. 8.

Molecular dynamic simulations

Molecular dynamic simulation was carried out for the chosen derivatives, considering the filtering process of the

top ten compounds based on their interaction profile and structural similitude. Seven compounds were chosen for *Tc*TR/*Hs*GR analysis, six for *Tv*TIM/*Hs*TIM, and nine compounds for *Fh*CatL/*Hs*CatL; compounds are identified with bold labels in Figs. 2, 4, and 7 for *Tc*TR, *Tv*TIM, and *Fh*CatL respectively.

***Tc*TR/*Hs*GR**

RMSD analysis

A full list of RMSD fluctuation values and graphs may be consulted in the supplementary material. Figure 9a shows the RMSD fluctuations for the most stable quinoxaline-*Tc*TR complexes: Zn_C38-*Tc*TR complex, Lit_C777-*Tc*TR, and free *Tc*TR. The most stable complex Zn_C38-*Tc*TR had a maximum fluctuation of 6.03 Å with a mean of 4.11 ± 0.47 Å as opposed to 2.42 Å with a mean of 1.77 ± 0.14 Å for free *Tc*TR, whereas Lit_C777-*Tc*TR complex had a maximum fluctuation of 9.89 Å with a mean of 5.30 ± 1.64 Å. Both complexes show that at the last 40 ns their fluctuations neared 4–5 Å, the least fluctuation observed for these dynamics. Figure 9b shows the *Hs*GR counterpart for these compounds' dynamics: Zn_C38-*Hs*GR complex, Lit_C777-*Hs*GR, and free *Hs*GR. Zn_C38-*Hs*GR complex had maximum fluctuation of 7.8 Å with a mean of 3.72 ± 0.57 Å, as opposed to 3.11 Å with a mean of 2.45 ± 0.39 Å for free

*Hs*GR, whereas Lit_C777-*Hs*GR complex had a maximum fluctuation of 6.08 Å with a mean of 4.72 ± 0.40 Å. Aside from a spike within the first 10 ns of the Zn_C38-*Hs*GR complex dynamics, the RMSD fluctuates very little from 3 to 4 Å the remaining dynamic. The Lit_C777-*Hs*GR complex fluctuates most of the dynamic between 5 and 6 Å. Analysis of RMSD values obtained for *Tc*TR and *Hs*GR complexes showed that all *Hs*GR-ligand complexes were more stable than *Tc*TR-ligand complexes.

RMSF analysis

A full list of RMSF fluctuation values and graphs may be consulted in the supplementary material. Figure 10a shows RMSF fluctuations for quinoxaline-*Tc*TR complexes: Zn_C38-*Tc*TR complex, Lit_C777-*Tc*TR, and free *Tc*TR, and Fig. 10b shows quinoxaline-*Hs*GR complexes: Zn_C38-*Hs*GR complex, Lit_C777-*Hs*GR, and free *Hs*GR. RMSF graphs for TR and GR show minor fluctuations located at loop regions prone to fluctuations. Still proteins remain mostly stable through the dynamics suggesting that ligand interaction did not considerably affect the protein.

The most notable observation may be attributed to the RMSF for *Hs*GR at about residues 318–368, where it may be observed that both ligand–protein complexes, Lit_C777 and Zn_C38, have a slightly lower RMSF than

Fig. 8 Representative interactions with cathepsin L for the libraries analyzed by molecular docking: top left literature, top right ZINC15, and bottom PubChem: dotted black line hydrophobic interaction, solid blue line hydrogen bond, and dotted orange line π -cation interaction

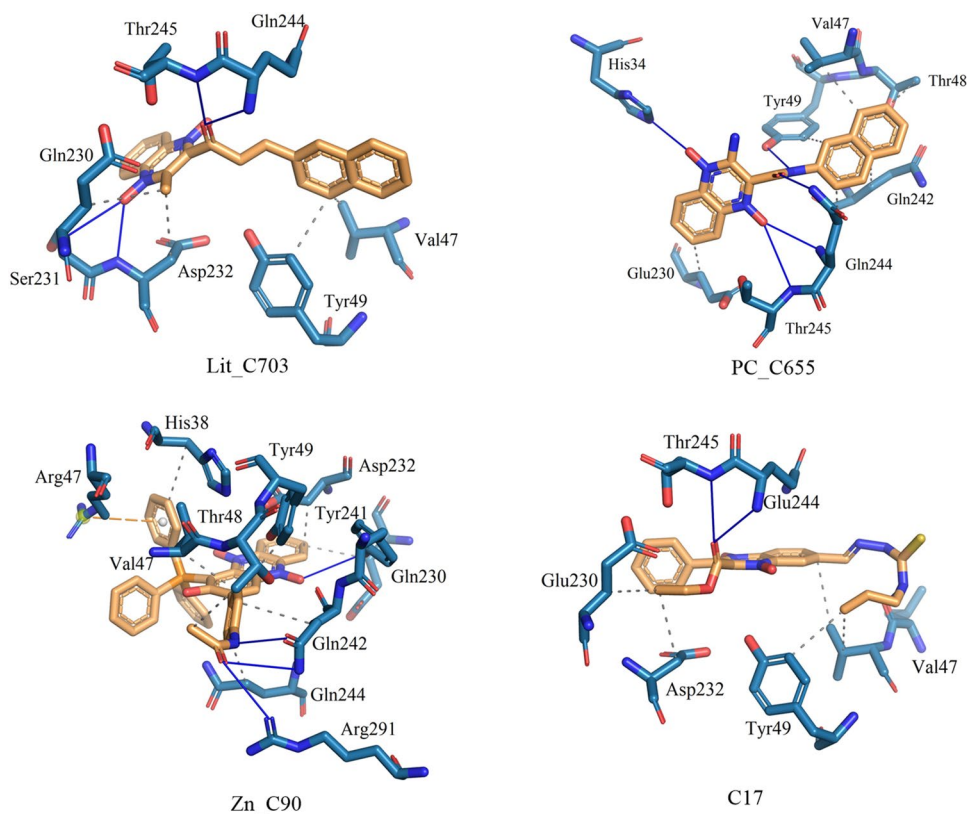
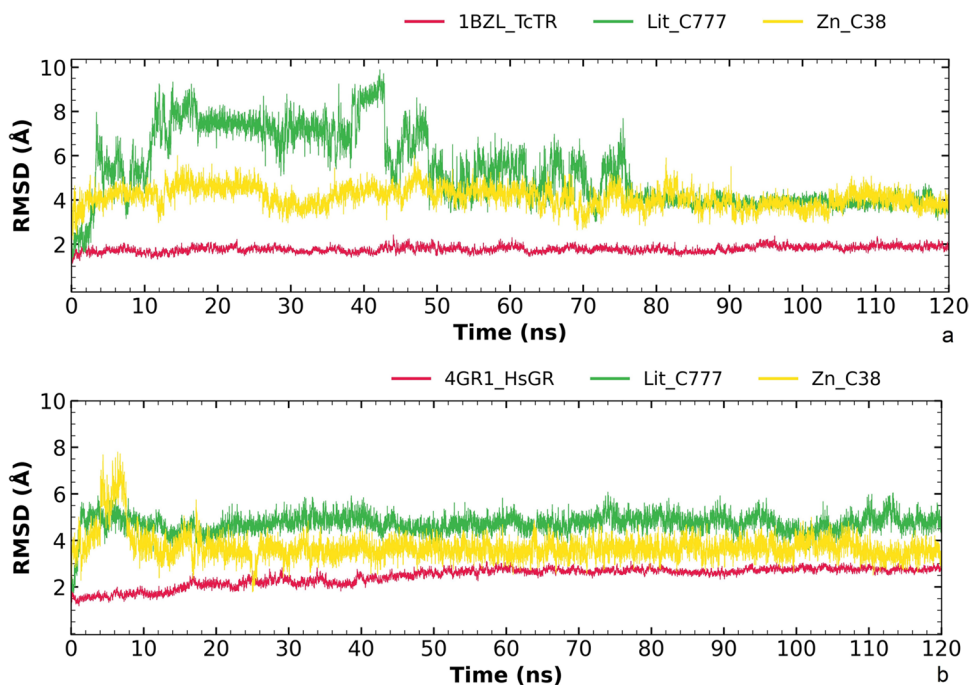


Fig. 9 RMSD graph for fluctuations overtime for *Tc*TR and *Hs*GR. **a** fluctuation of Lit_C777-*Tc*TR (0.69–9.89 Å), Zn_C38-*Tc*TR (0.38–6.03 Å), and free *Tc*TR (0.32–2.42 Å); **b** Lit_C777-*Hs*GR (0.72–6.08 Å), Zn_C38-*Hs*GR (0.51–7.8 Å), and free *Hs*GR (0.33–3.11 Å)



protein alone, suggesting a more stable position of the residues during analysis of the dynamics, again indicating that it is predicted that this type of compounds may behave with a slight preference toward human GR.

The radius of gyration analysis

A full list of radius of gyration values and graphs may be consulted in the supplementary material. Figure 11a shows the radius of gyration for Lit_C777-*Tc*TR and Zn_C38-*Tc*TR complexes, and Fig. 11b shows the radius of gyration for Lit_C777-*Hs*GR and Zn_C38-*Hs*GR complexes. Complexes remain stable throughout the 120 ns of molecular dynamics with minimal fluctuation; comparing receptor to complexes, there is not a significant difference which suggests that protein remains compact in its dynamics, meaning that any RMSD fluctuations are due to ligand binding instability not protein derived.

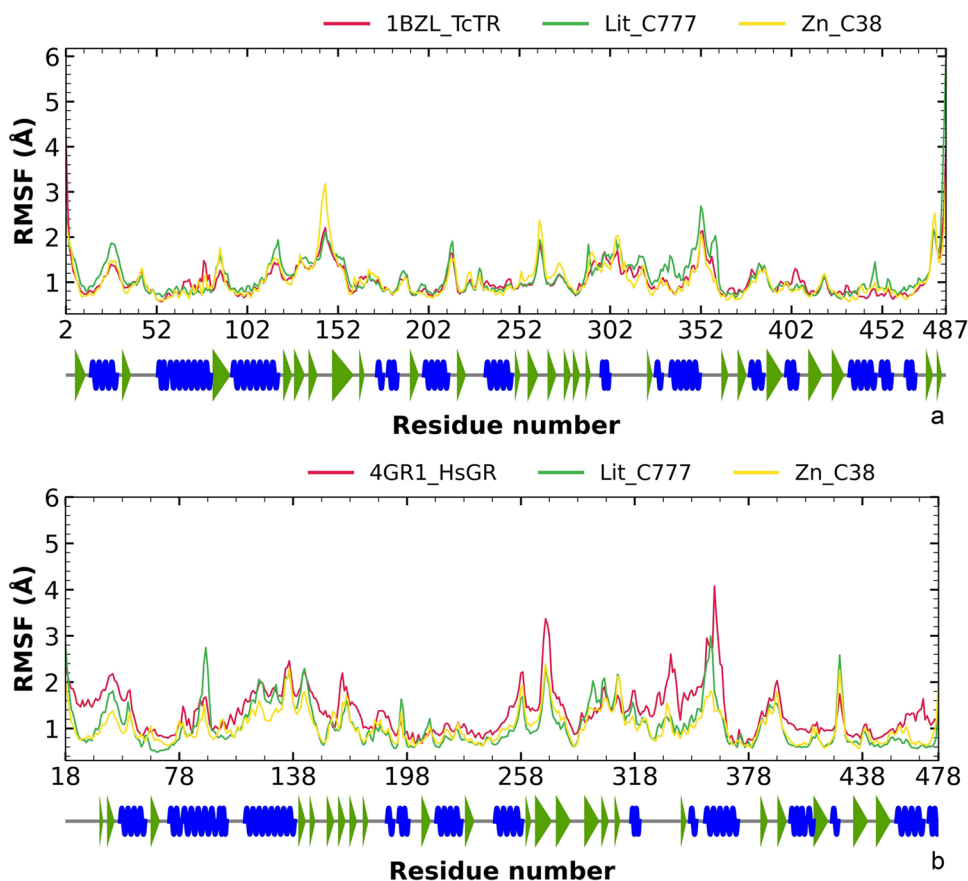
Contact analysis of trajectory

The residue interaction frequency and the ligand-residue interaction mapping observed for the last third of the dynamics' trajectory with *Tc*TR/*Hs*GR for Lit_C777 and Zn_C38 are presented in Figs. 12 and 13, respectively.

Interaction analysis provides a clearer picture as to where the ligand moved toward to complement the RMSD analysis. As it may be observed in Fig. 12, the most common interactions held by Lit_C777 during the last 40 ns of the

molecular dynamics' trajectory include residues belonging to the denominated Z-site: Pro398, Leu399, and γ -Glu-site Glu466 and His461, being this last residue part of the catalytic triad for *Tc*TR. The interactions with the Z-site were mapped to the pyrazine portion of the quinoxaline ring and an N–O group; in the case of the γ -Glu-site, Glu466 hydrogen bonding occurs with the amide group present in the linking chain between the quinoxaline and the indole ring while His461 interacts with the sulfur atom in the middle of this same linking chain. This binding pattern may be considered akin to the binding of TS₂ as hydrophobic residue host of the mostly hydrophobic portion of the ligand and a sulfur atom is oriented toward the His461 residue. These results further support the hypothesis that Lit_C777 has the potential to behave as a *Tc*TR inhibitor as the predicted interactions for 4000 frames point toward the blocking of important residues for the binding and catalysis of the natural ligand TS₂. Further analyzing the types of interactions that may be observed for this ligand, it was calculated that Lit_C777 holds in an average of 2.387 hydrogen bonds per frame; a graph of the number of hydrogen bonds over the full length of the dynamics' trajectory may be consulted in supplementary material. Under the same type of analysis and during the same trajectory portion of the molecular dynamics' simulation Zn_C38 shows interactions with residues belonging to hydrophobic cleft: Tyr11, Z-site: Leu399, and with two residues belonging to the catalytic triad: His461 and Cys58. For this ligand, it may be observed that the interaction mapping includes multiple hydrophobic interactions along the quinoxaline ring analog and the phenylpiperazine group oriented toward the

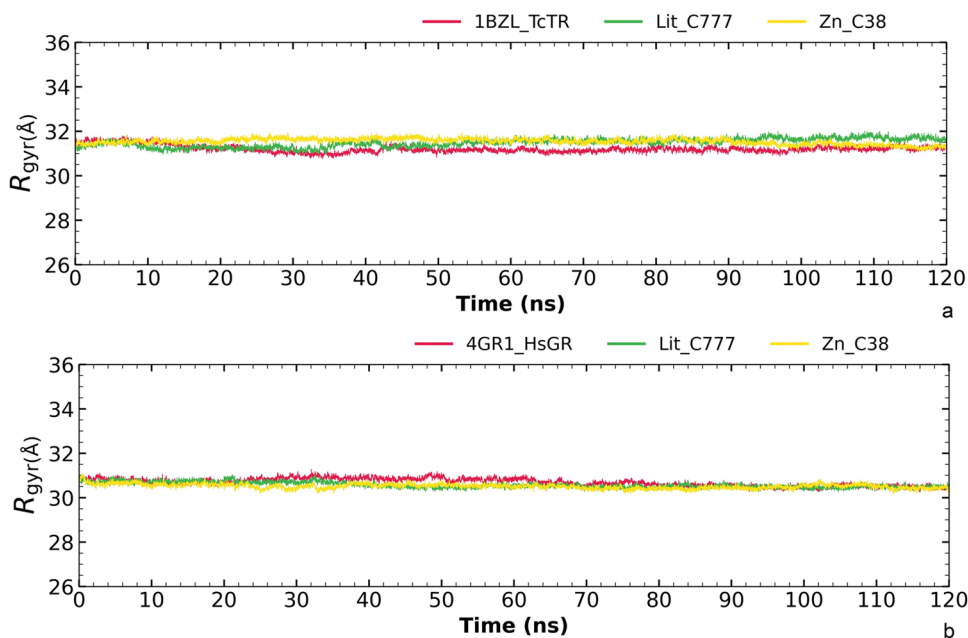
Fig. 10 **a** RMSF graph for fluctuations overtime for Lit_C777-*Tc*TR and Zn_C38-*Tc*TR complexes. **b** RMSF graph for fluctuations overtime for Lit_C777-*Hs*GR and Zn_C38-*Hs*GR complexes, blue spiral (alpha helix), green triangle (beta sheet), and in between space (loop)



catalytic triad where it interacts with His461 and Cys58. As such, this ligand shows a high potential to act as a *Tc*TR inhibitor, as it may potentially block two crucial ligands for its functioning. In the case of Zn_C38, the hydrogen bond

analysis showed that it has an average of 0.818 hydrogen bonds per frame which can be attributed to the low number of polar bonds present in the molecule. Supplementary material may be consulted for full trajectory graph.

Fig. 11 **a** Radius of gyration graph for Lit_C777-*Tc*TR and Zn_C38-*Tc*TR complexes. **b** Radius of gyration graph for Lit_C777-*Hs*GR and Zn_C38-*Hs*GR complexes



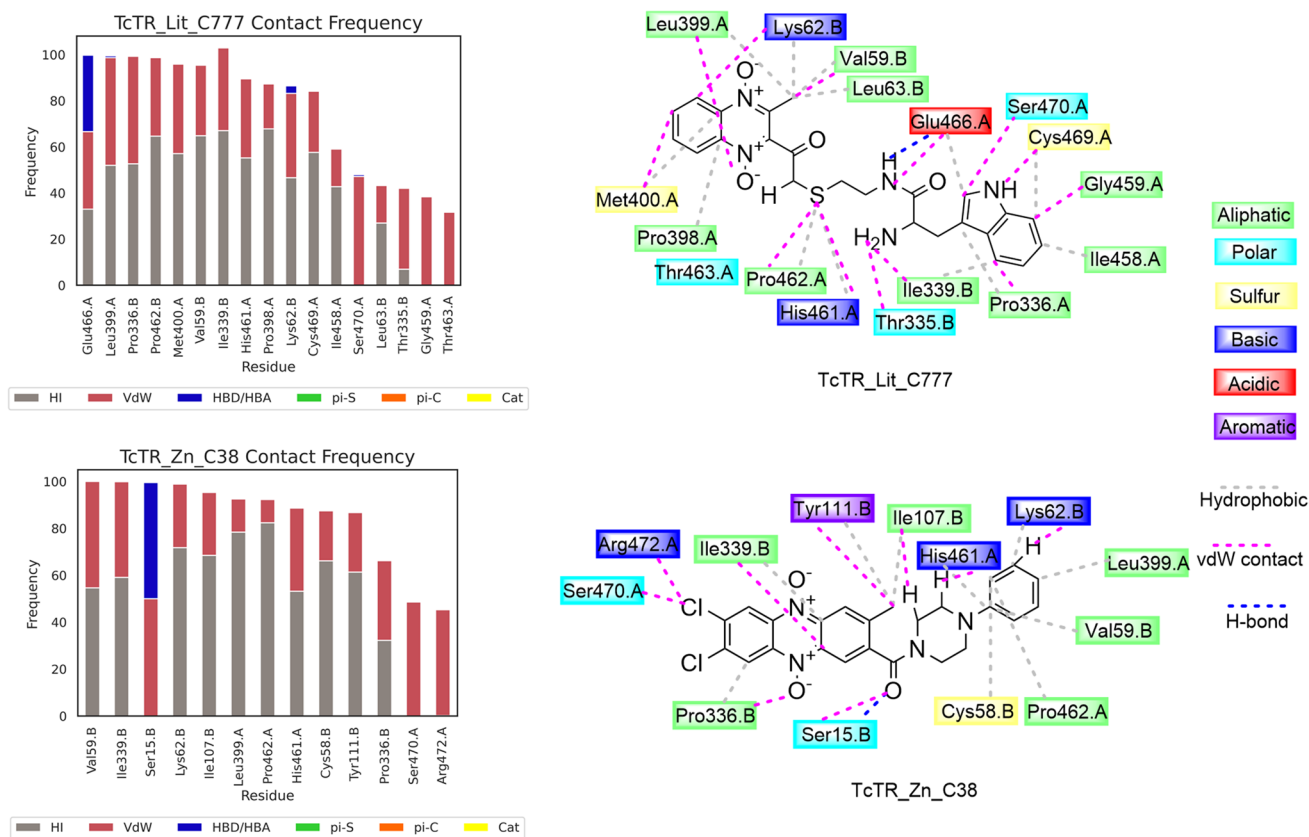


Fig. 12 Interaction frequencies and ligand-residue interaction map for MD simulations of *TcTR* complexes

As for assessing selectivity, the behavior observed for Lit_C777 resembles closely the interaction pattern observed for this ligand on *TcTR*; two highly frequent interactions occur with residues which 3D align to *TcTR* Z-site residues, Leu399^{*TcTR*}-Met406^{*HsGR*} and Phe396^{*TcTR*}-Phe403^{*HsGR*}, hydrophobic cleft residues Tyr111^{*TcTR*}-Tyr114^{*HsGR*}, and Trp22^{*TcTR*}-Arg37^{*HsGR*}, and γ -Glu-site residues Glu467^{*TcTR*}-Glu473^{*HsGR*}, and His461^{*TcTR*}-His467^{*HsGR*} (a catalytic triad residue). The interaction mapping is distinct to its binding to *TcTR*; in this case, indole ring holds the Z-site interactions, and the quinoxaline ring interacts at the hydrophobic cleft; the interaction of His467 is maintained at the sulfur atom in the middle of the linking chain. Thus, it was suggested that Lit_C777 may act as an inhibitor for both proteins. The hydrogen bond number analysis for Lit_C777 on *HsGR* shows an average of 1.125 hydrogen bonds per frame, slightly less than half of what was observed for the *TcTR* simulation which may suggest that *TcTR* is still a better target for Lit_C777 than *HsGR*. A similar interaction pattern was observed for Zn_C38, where this ligand is predicted to interact with residues which 3D align with residues belonging to the hydrophobic cleft of *TcTR*, Trp22^{*TcTR*}-Arg37^{*HsGR*}, Tyr111^{*TcTR*}-Tyr114^{*HsGR*}, and Met114^{*TcTR*}-Asn117^{*HsGR*}, Z-site Leu399^{*TcTR*}-Met406^{*HsGR*},

and catalytic residue His461^{*TcTR*}-His467^{*HsGR*}; in this case, only one of three catalytic residues as opposed to the interactions is seen for Zn_C38 on *TcTR* which holds two such interactions. Like the contrasting mapping of interactions for Lit_C777 with both proteins, the mapping of Zn_C38 for *HsGR* shows this reverse interaction map, where phenylpiperazine group and part of the quinoxaline ring hold hydrophobic interactions and orient the quinoxaline ring toward the vicinity of the catalytic triad which permit the interaction of His467 with this ring. As for the hydrogen bond, number analysis for Zn_C38 on *HsGR* shows an average of 0.109 hydrogen bonds per frame, nearly inexistent about eight times less than what was observed for *TcTR*, which may suggest that *TcTR* is still a better target for Zn_C38 than *HsGR*. Altogether, these predicting analyses suggest that though these interacting behaviors seem unselective, there is still a higher tendency toward *TcTR* over *HsGR*.

MMPBSA

$\Delta G_{binding}$ for each complex, as calculated by the MMPBSA method, is presented in Table 2. It may be observed that in both cases, quinoxaline derivatives are scored with higher affinity toward *TcTR* over *HsGR*, strengthening the notion that these

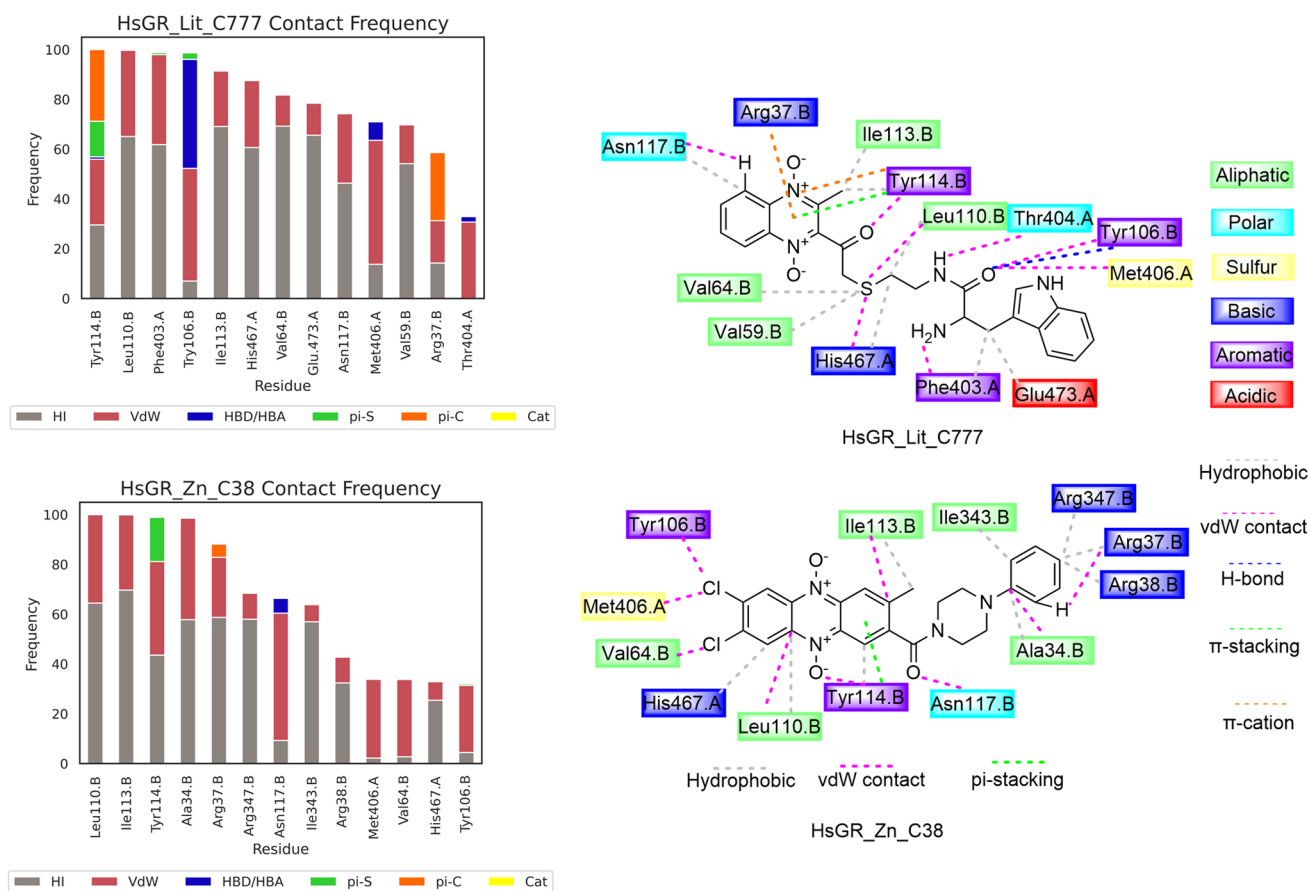


Fig. 13 Interaction frequencies and ligand-residue interaction map for MD simulations of *HsGR* complexes

derivatives may be candidates for *TcTR* inhibition. As it may be observed in Fig. 14, for Lit_C777, the same three equivalent residues have a repulsive energy contribution to these interactions: Glu466/472, Glu467/473, and Lys62/67 for *TcTR/HsGR*, respectively. Still, in the case of attractive contributions for Lit_C777 on *HsGR*, these are in the hydrophobic cleft, whereas for *TcTR* at the Z-site and even with catalytic residue His461. In the case of Zn_C38, the energy contribution for the residues participating in the binding of the ligand to the protein has a similar pattern for both *TcTR* and *HsGR*. In both cases, a charged amino acid residue acts as a source of repulsive energy contribution, and mainly aliphatic residues act as attractive energy contributors. The difference resides in the location of these participating residues. In the case of *HsGR*, it is solely at the hydrophobic cleft region, and for *TcTR*, it involves not only aliphatic residues but also charged residue Glu466 part of the γ -Glu site near catalytic

residue His461. This energy distribution analysis adds support to the prediction that both these compounds can act as *TcTR* inhibitors preferred over *HsGR*.

TvTIM/HsTIM

RMSD analysis

A full list of RMSD fluctuation values and graphs may be consulted in the supplementary material. Figure 15a shows the RMSD fluctuations for the most stable quinoxaline-TvTIM complexes: Lit_C208-TvTIM complex, Zn_C76-TvTIM, and free TvTIM. The most stable complex Lit_C208-TvTIM had a maximum fluctuation of 9.82 Å, with a mean of 6.38 ± 1.84 Å as opposed to 2.47 Å with a mean of 1.84 ± 0.19 for free

Table 2 Binding energy components for *TcTR* and *HsGR* complexes with Lit_C777 and Zn_C38 in kcal/mol

	ΔE_{elec}	ΔE_{vdW}	ΔG_{polar}	$\Delta G_{nonpolar}$	$\Delta G_{binding}$
<i>TcTR</i> _Lit_C777	-20.38 ± 0.34	-61.89 ± 0.33	60.25 ± 0.5	-5.46 ± 0.02	-27.48 ± 0.27
<i>HsGR</i> _Lit_C777	-15.24 ± 0.24	-50.76 ± 0.27	50.12 ± 0.49	-4.89 ± 0.03	-20.77 ± 0.31
<i>TcTR</i> _Zn_C38	-5.8 ± 0.1	-45.24 ± 0.25	21.74 ± 0.2	-4.76 ± 0.02	-34.07 ± 0.26
<i>HsGR</i> _Zn_C38	-3.89 ± 0.1	-44.11 ± 0.21	21.09 ± 0.2	-4.56 ± 0.02	-31.47 ± 0.21

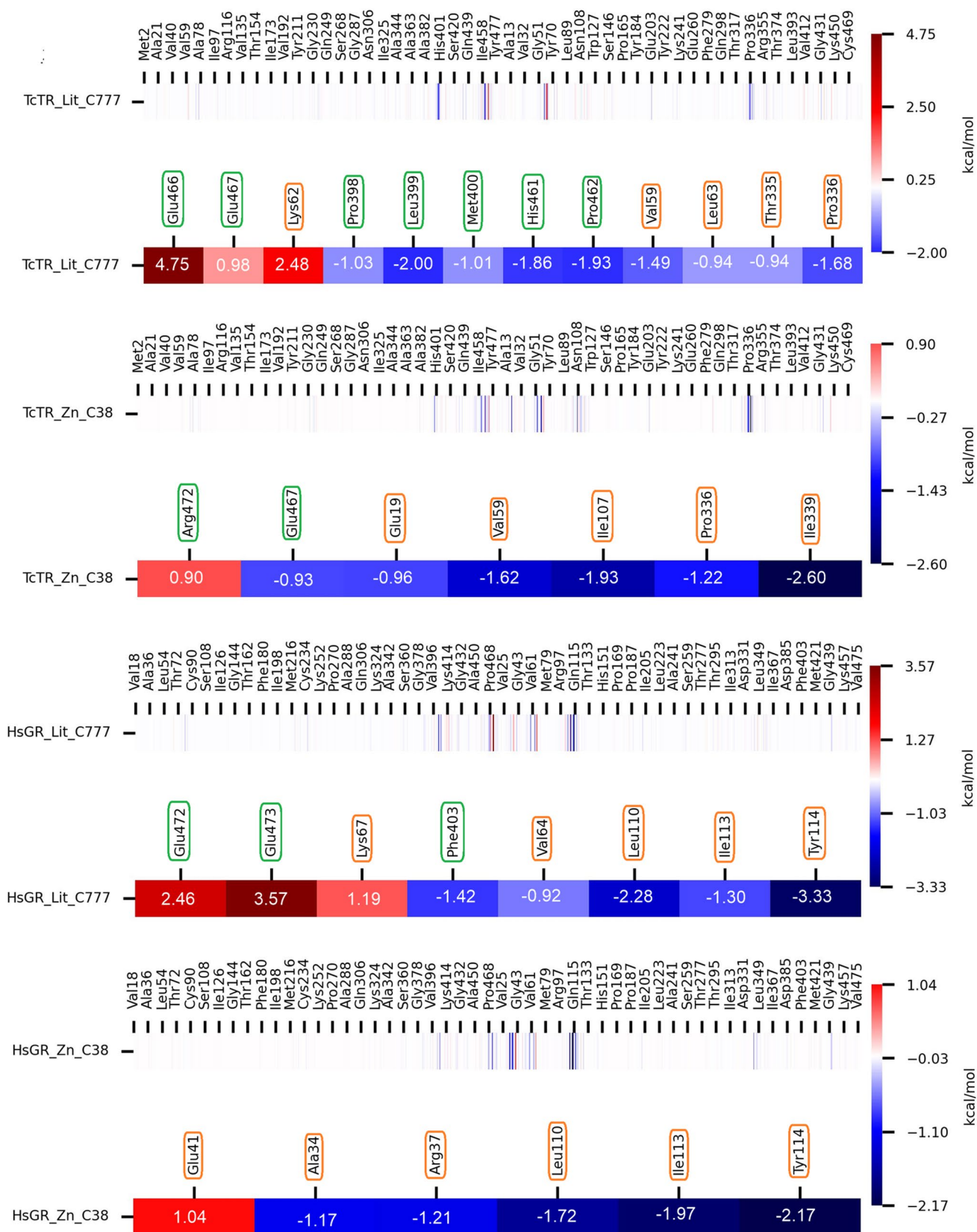


Fig. 14 Per-residue energy contribution for *TcTR* and *HsGR* complexes (chain A green, chain B orange)

TvTIM, whereas *Zn_C76-TvTIM* complex had a maximum fluctuation of 19.8 Å with a mean of 13.29 ± 3.87 Å. For *Lit_C208* beyond 15 ns, fluctuation spikes and remains fluctuating around 8 Å, and *Zn_C76* remains going further as the dynamic's simulation progresses until reaching nearly 20 Å. As for the counterpart in Fig. 15b, *Lit_C208-HsTIM*, it spikes and remains fluctuating beyond 20 Å with a mean of 23 ± 2.80 Å. On the other hand, *Zn_C76-HsTIM* remains fluctuating with an RMSD around 4 Å with a maximum fluctuation of 4.05 Å with a mean of 3.28 ± 0.18 Å, as opposed to free *HsTIM* with a maximum fluctuation of 2.76 Å with a mean of 1.80 ± 0.32 Å. All but one compound showed a more stable complex for the human homolog rather than the target parasite protein, suggesting a possible inhibition favored toward the host rather than the pathogen.

RMSF analysis

A full list of RMSF fluctuation values and graphs may be consulted in the supplementary material. Figure 16a shows RMSF fluctuations for quinoxaline-*TvTIM* complexes: *Zn_C76-TvTIM* complex, *Lit_C208-TvTIM*, and free *TvTIM*. Complex behavior resembles that of the receptor alone. The fluctuation seen is located at a loop region around residues 67–77. Still, it is more pronounced that fluctuations seen in the receptor alone warrant further study at determining such pronounced fluctuation. Similarly, fluctuations around residues 127–142 and 217–227 can be observed in regions of alpha-helix secondary structure which deems them even more important since these regions do not have as high a fluctuation pattern as loop regions. Altogether,

indicating that the observation of the RMSD being unstable is confirmed by this instability in RMSF.

Figure 16b shows quinoxaline-*HsTIM* complexes: *Zn_C76-HsTIM* complex, *Lit_C208-HsTIM*, and free *HsTIM*. In the case of *HsTIM*, there are similar fluctuations as compared to the receptor alone. Still, it is possible to note that for the most stable complex with *Zn_C76* there are instances of both decreased stabilities as is the case of the region around residues 133–143, as well as increased stability as in the case of regions around residues 168–178 and 208–223. The case of decreased stability is in the alpha helix region, and the increased stability in the loop-alpha helix regions.

The radius of gyration analysis

A full list of radius of gyration values and graphs may be consulted in the supplementary material. Figure 17a shows the radius of gyration for *Lit_C208-TvTIM* and *Zn_C76-TvTIM* complexes, and Fig. 17b shows the radius of gyration for *Lit_C208-HsTIM* and *Zn_C76-HsTIM* complexes. Complexes remain stable throughout the 120 ns of molecular dynamics with a minimal fluctuation; comparing receptor to complexes, there is not a major difference which suggests that protein remains compact in its dynamics, meaning that any RMSD fluctuations are due to ligand binding instability not protein derived.

Contact analysis of trajectory

The residue interaction frequency and the ligand-residue interaction mapping observed for the last third of the

Fig. 15 RMSD graph for fluctuations overtime for *TvTIM* and *HsTIM*. **a** fluctuation of *Lit_C208-TvTIM* (0.57–9.82 Å), *Zn_C76-TvTIM* (0.59–19.8 Å), and free *TvTIM* (0.29–2.47 Å); **b** *Lit_C777-HsTIM* (0.74–28.52 Å), *Zn_C38-HsTIM* (0.68–4.05 Å), and free *HsTIM* (0.32–2.76 Å)

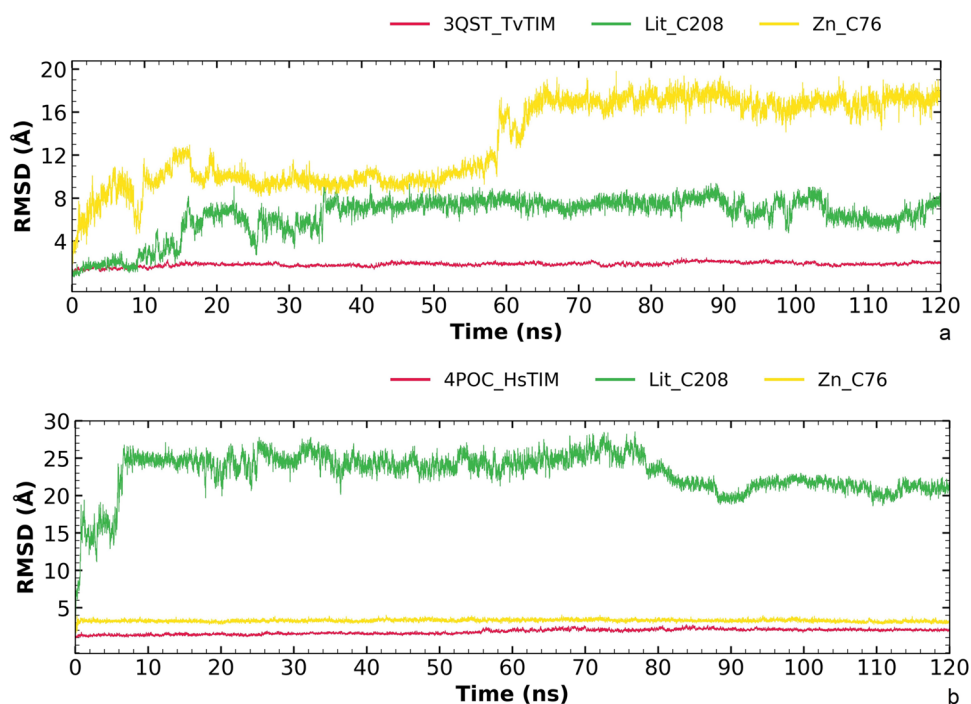
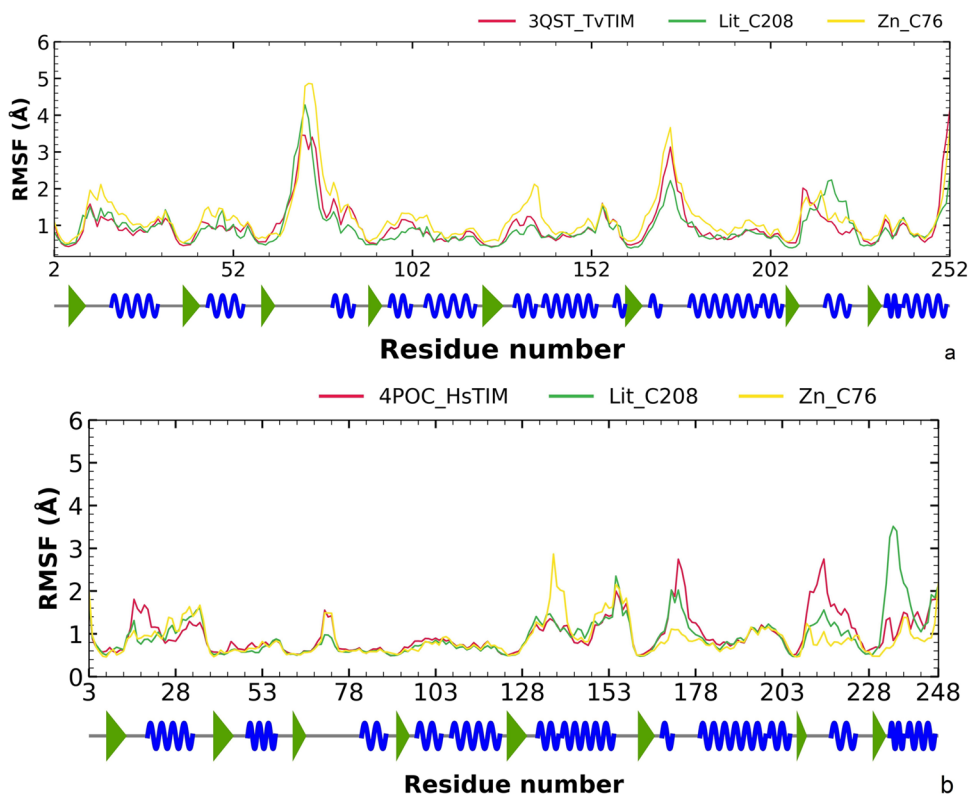


Fig. 16 **a** RMSF graph for fluctuations overtime for Lit_C208-*Tv*TIM and Zn_C76-*Tv*TIM complexes; **b** RMSF graph for fluctuations overtime for Lit_C208-*Hs*TIM and Zn_C76-*Hs*TIM complexes, blue spiral (alpha helix), green triangle (beta sheet), and in between space (loop)

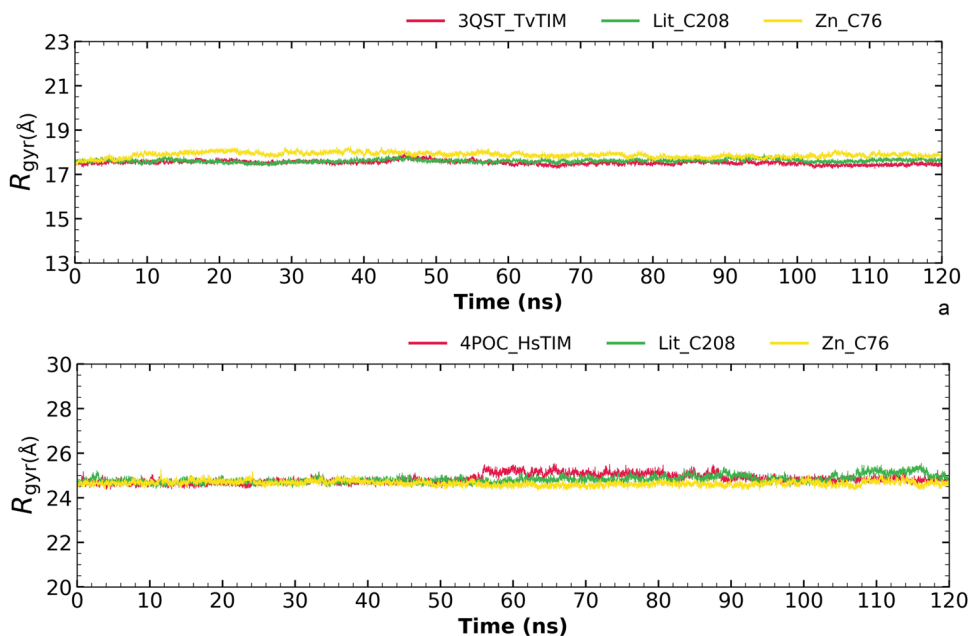


dynamics' trajectory with *Tv*TIM/*Hs*TIM for Lit_C208 and Zn_C76 are presented in Figs. 18 and 19.

Interaction analysis provides a clearer picture as to where the ligand moved toward to complement the RMSD analysis. As it may be observed in Fig. 18, the most common interactions present for Lit_C208 during the last

40 ns of the molecular dynamics' simulation include two residues of importance: His94 and Glu96, the former part of the catalytic dyad and the latter reported to play an important role in the catalytic activity even if not participating actively. The mapping of the observed interactions places the quinoxaline N–O bond interacting with Glu96

Fig. 17 **a** Radius of gyration graph for Lit_C208-*Tv*TIM and Zn_C76-*Tv*TIM complexes. **b** Radius of gyration graph for Lit_C208-*Hs*TIM and Zn_C76-*Hs*TIM complexes



and the ring of the nitrophenyl group oriented toward the His94; additionally Asn9, which is near Lys11, the second catalytic residue, is mapped to interact with the nitro group. This information gathered from 4000 frames over a span of 40 ns supports the hypothesis that Lit_C208 may act as a TvTIM inhibitor by blocking the access of the natural ligand to the catalytic residues. The hydrogen bond count for the molecular dynamics' simulation averages 3.458 hydrogen bonds per frame which suggests a high potential to remain bound and behave as an inhibitor if such bonds are formed with residues of importance, in this case Glu96 is predicted to hold such interaction. As for Zn_C76, all interactions observed for this ligand over the last 40 ns are far away from any TvTIM catalytic residue making the predicted inhibitory potential for this ligand very low. Hydrogen bond number analysis for this ligand shows that it holds an average of 0.954 hydrogen bonds per frame, which suggests a low stability potential.

As for selectivity toward TvTIM over HsTIM, while Lit_C208 holds a trajectory that permits interactions with one of two catalytic residues for TvTIM, this ligand holds

a trajectory for HsTIM that does not permit any interaction with residues in the vicinity of the catalytic dyad. It holds an average of 3.342 hydrogen bonds per frame, but these are with residues away from the catalytic dyad, thus suggesting a low potential to HsTIM inhibition. Conversely, Zn_C76 for TvTIM holds all its interactions far from the catalytic dyad, for HsTIM the most common observed interaction is Lys13, which is the 3D aligned corresponding residue to TvTIM catalytic dyad residue Lys11, making this ligand a potential inhibitor but for HsTIM not TvTIM. The average number of hydrogen bonds made by Zn_C76 with HsTIM is 2.919; still most of these are away from catalytic residues. The groups responsible for the favorable interactions with catalytic residue Lys13 and nearby residues are the quinoxaline ring as it may be observed in Fig. 19.

MMPBSA

The $\Delta G_{binding}$ observed for Lit_C208 as calculated for MMPBSA, as presented in Table 3, showed that the affinity for this ligand is better toward TvTIM over HsTIM, which

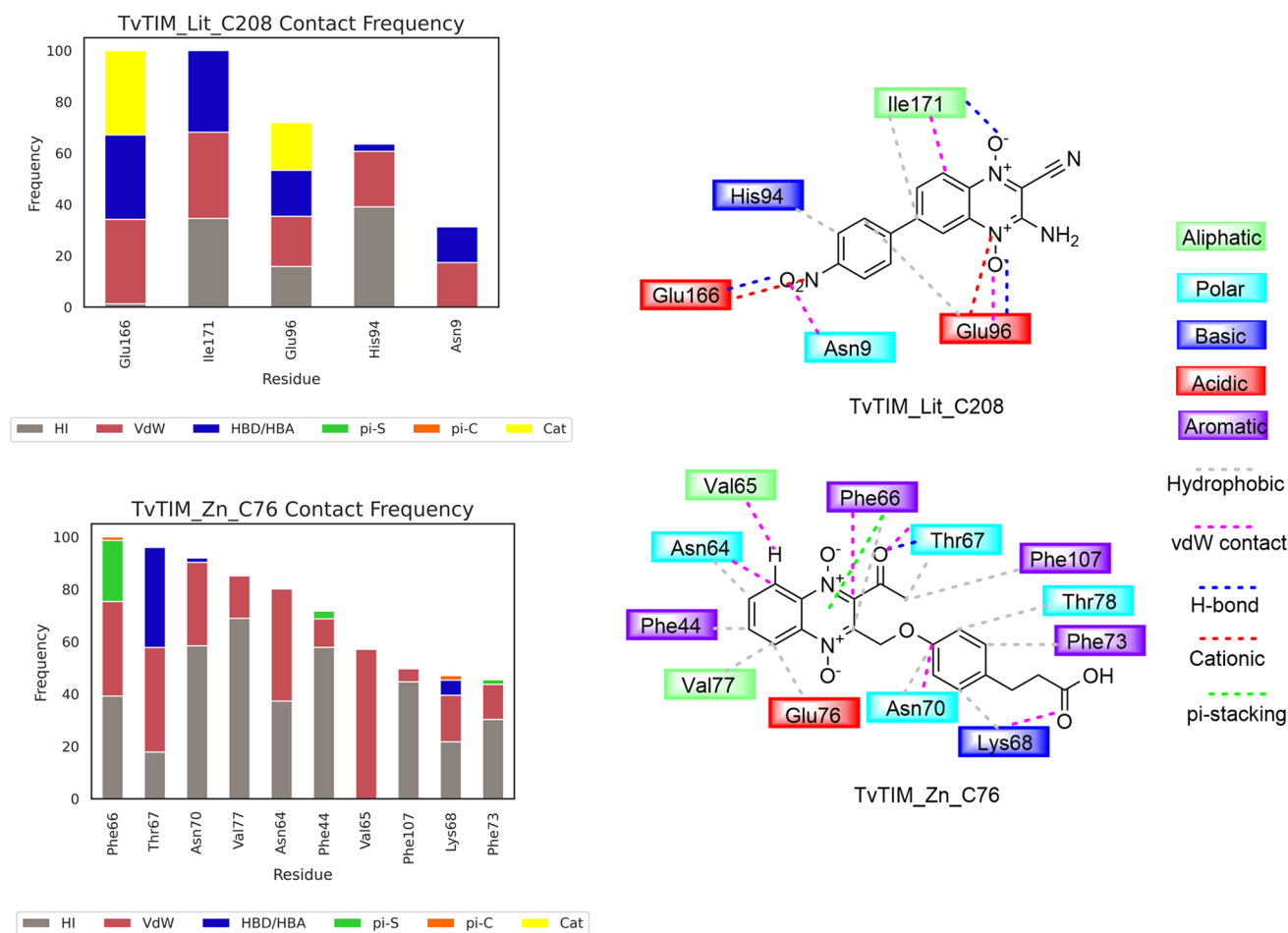


Fig. 18 Interaction frequencies and ligand-residue interaction map for MD simulations of TvTIM complexes

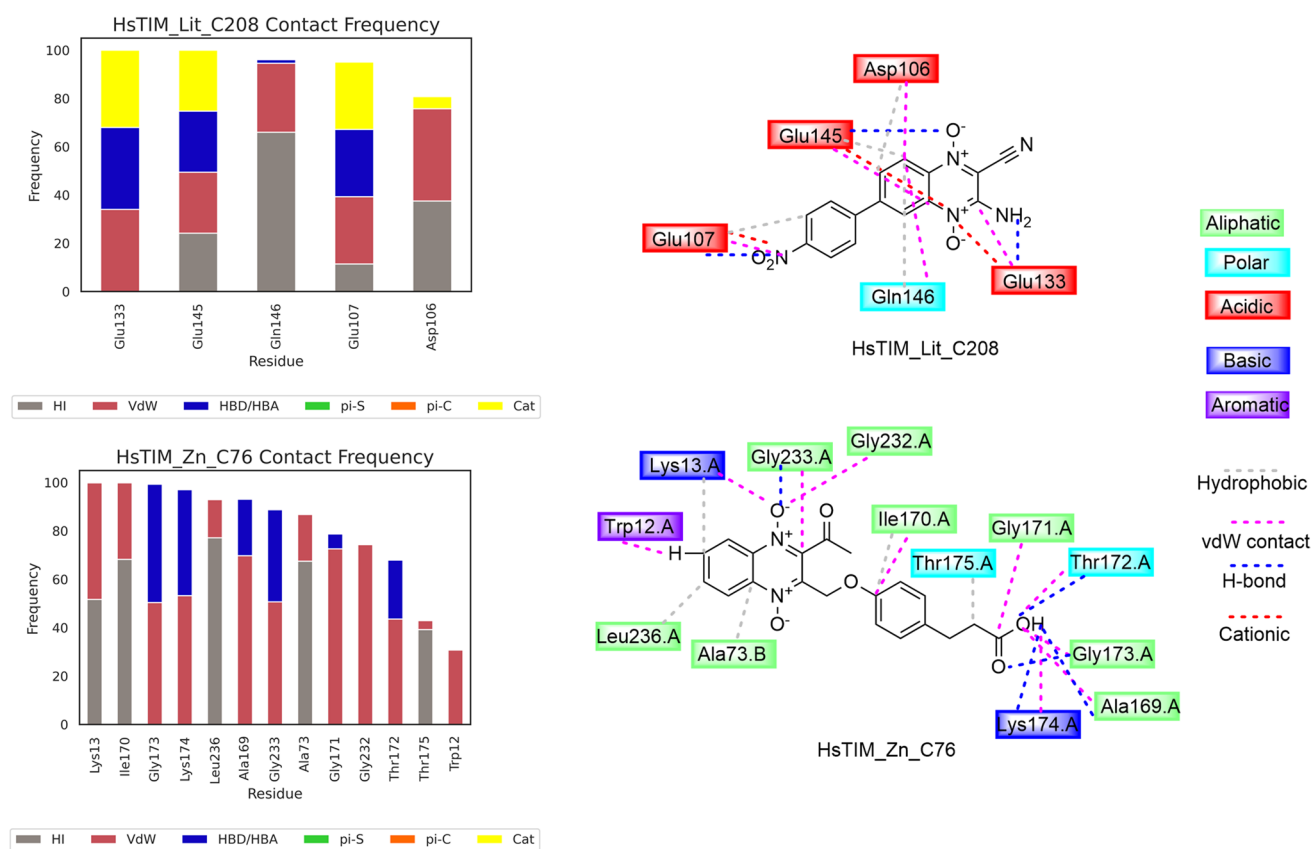


Fig. 19 Interaction frequencies and ligand-residue interaction map for MD simulations of *HsTIM* complexes

further emphasizes the potential that it possesses to behave as a *TvTIM* inhibitor. The per-residue energy decomposition showed that the main residues providing attractive energy include Glu96, Glu166, and Glu63 which surround the catalytic dyad; Lys11 provides a strong repulsive contribution and His94 only very slightly attractive which is consistent with the interaction pattern observed for this ligand, which is still in line with its potential as a *TvTIM* inhibitor. MMPBSA analysis with Lit_C208 on *HsTIM* shows that the main attractive contributions are with residues Glu145, Asp106, Asp132, Asp152, and Glu104 which point away from the catalytic residues, which provide further support towards the hypothesis of selective inhibition of *TvTIM*. Conversely, Zn_76 shows a binding energy slightly favoring *HsTIM*. Additionally, the residues contributing attraction for the binding of Zn_C76 in *TvTIM* are away from the

catalytic dyad. On the other hand, the residues contributing attraction for Zn_C76 on *HsTIM* point toward the catalytic dyad, thus suggesting that Zn_C76 may potentially act as a *HsTIM* inhibitor instead of *TvTIM*; Fig. 20 shows the most highly contributing residues both for attraction and repulsion for Zn_C76; Lit_C208 may be consulted in Supplementary material as MMPBSA predicted many contributing residues that are thus unable to be properly displayed in a small figure.

FhCatL/HsCatL

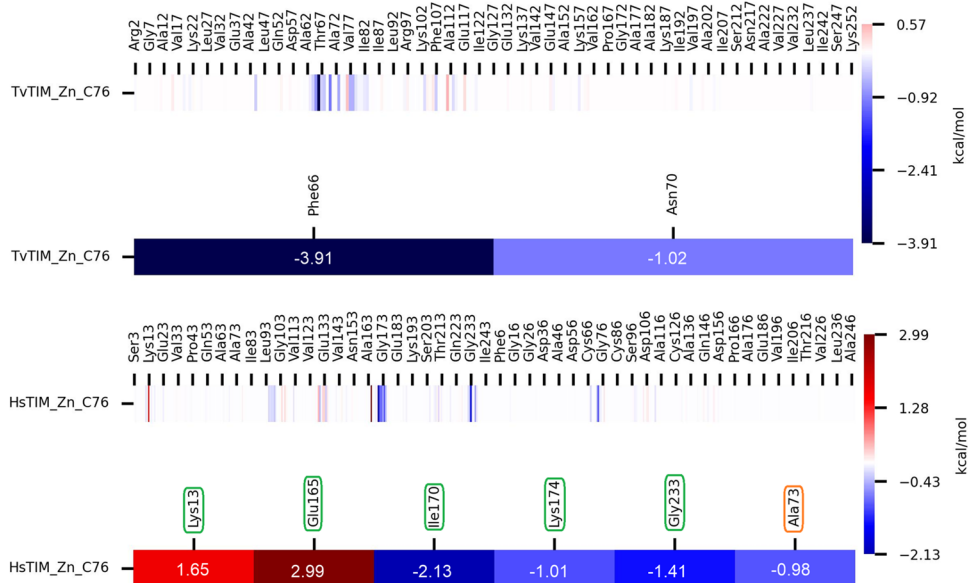
RMSD analysis

A full list of RMSD fluctuation values and graphs may be consulted in the supplementary material. Figure 21a shows the RMSD fluctuations for the most stable

Table 3 Binding energy components for *TvTIM* and *HsTIM* complexes with Lit_C208 and Zn_C76 in kcal/mol

	ΔE_{elec}	ΔE_{vdW}	ΔG_{polar}	$\Delta G_{nonpolar}$	$\Delta G_{binding}$
<i>TvTIM</i> _Lit_C208	-196.95 ± 1.57	-12.77 ± 0.38	139.78 ± 1.2	-2.85 ± 0.01	-72.76 ± 0.64
<i>HsTIM</i> _Lit_C208	-263.52 ± 1.56	-7.52 ± 0.35	203.27 ± 1.31	-2.77 ± 0.02	-70.57 ± 0.73
<i>TvTIM</i> _Zn_C76	-9.96 ± 0.29	-32.5 ± 0.32	26.42 ± 0.5	-3.3 ± 0.03	-19.33 ± 0.37
<i>HsTIM</i> _Zn_C76	-16.47 ± 0.13	-37.12 ± 0.18	37.79 ± 0.25	-3.85 ± 0.01	-19.64 ± 0.26

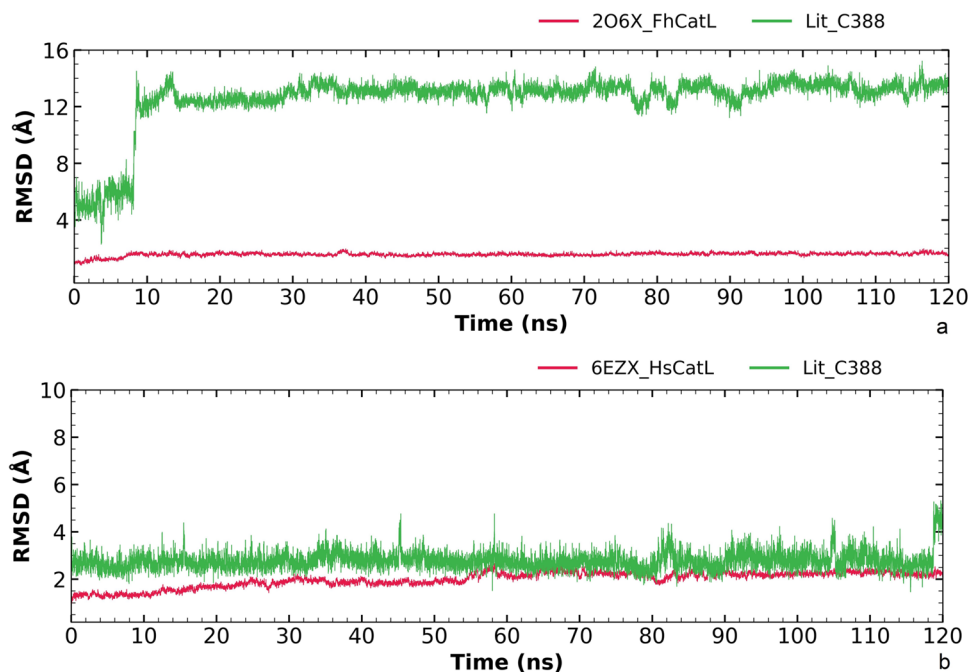
Fig. 20 Per-residue energy contribution for *Tv*TIM and *Hs*TIM complexes (chain A green, chain B orange)



quinoxaline-*Fh*CatL complex: Lit_C388-*Fh*CatL complex had a maximum fluctuation of 15.22 Å, with a mean of 12.54 ± 2.00 Å and all other complexes higher than 20 Å maximum fluctuation, as opposed to free *Fh*CatL which had a maximum fluctuation of 1.97 Å with a mean of 1.56 ± 0.14 Å. The fluctuation for this complex spike around 8 ns and it remains fluctuating between 12 and 15 Å. As for the case of *Hs*CatL Fig. 21b, the fluctuation for the Lit_C388-*Hs*CatL complex had a maximum

fluctuation of 5.32 Å with a mean of 2.78 ± 0.38 Å, and for the *Hs*CatL free protein, it showed a maximum fluctuation of 2.67 Å with a mean of 1.99 ± 0.32 Å. From all tested proteins, this protein shows the least potential to be inhibited by quinoxaline derivatives. A possible explanation for this unstable behavior is that the site that was found by blind docking is a very superficial site structurally composed mainly of loops, which by themselves are already unstable structures.

Fig. 21 RMSD graph for fluctuations overtime for *Fh*CatL and *Hs*CatL. **a** Fluctuation of Lit_C388-*Fh*CatL (0.57–15.22 Å) and free *Fh*CatL (0.31–1.97 Å); **b** Lit_C388-*Hs*CatL (0.94–5.32 Å) and free *Hs*CatL (0.44–2.67 Å)



RMSF analysis

Figure 22a shows RMSF fluctuations for all complexes with *FhCatL*; this shows fluctuations at loop regions near residues 70–80 and 85–95 for complexes with compounds Lit_C654, PC_C655, and Zn_C90, a second loop region with high fluctuation occurred near residues 170–190 for complexes with compounds Lit_C388 and Zn_C12. Further analysis may permit a better understanding of the reasoning behind the effect.

Figure 22b focuses solely on the most stable complex formed with compound Lit_C388; it is possible to notice that for the most part the RMSF is unchanged from its apo state, which suggest minimal interference from the docked ligand. Still, it is possible to note that around residues 170–190, there is a considerable spike in the RMSF, which suggests a notorious increase instability for residues distant from the initial docking pose, which

coincide with the high RMSD observed for this ligand complex. Figure 22c shows the fluctuation for Lit_C388-*HsCatL*, like the *FhCatL*; the fluctuations are minimal in comparison to the apo protein; still it is possible to note a major fluctuation in the region around residues 91–101.

The radius of gyration analysis

A full list of radius of gyration values and graphs may be consulted in the supplementary material. Figure 23a shows the radius of gyration for *FhCatL*-Lit_C388 complex; similarly, Fig. 23b shows the radius of gyration for *HsCatL*-Lit_C388. Complexes remain stable throughout the 120 ns of molecular dynamics with a minimal fluctuation; comparing receptors to complexes, there is not a major difference which suggests that protein remains compact in its dynamics, meaning that any RMSD fluctuations are due to ligand binding instability not protein derived.

Fig. 22 a RMSF graph for fluctuations overtime for all *FhCatL*-ligand complexes, b RMSF graph for Lit_C388-*FhCatL* complex, and c Lit_C388-*HsCatL* complex

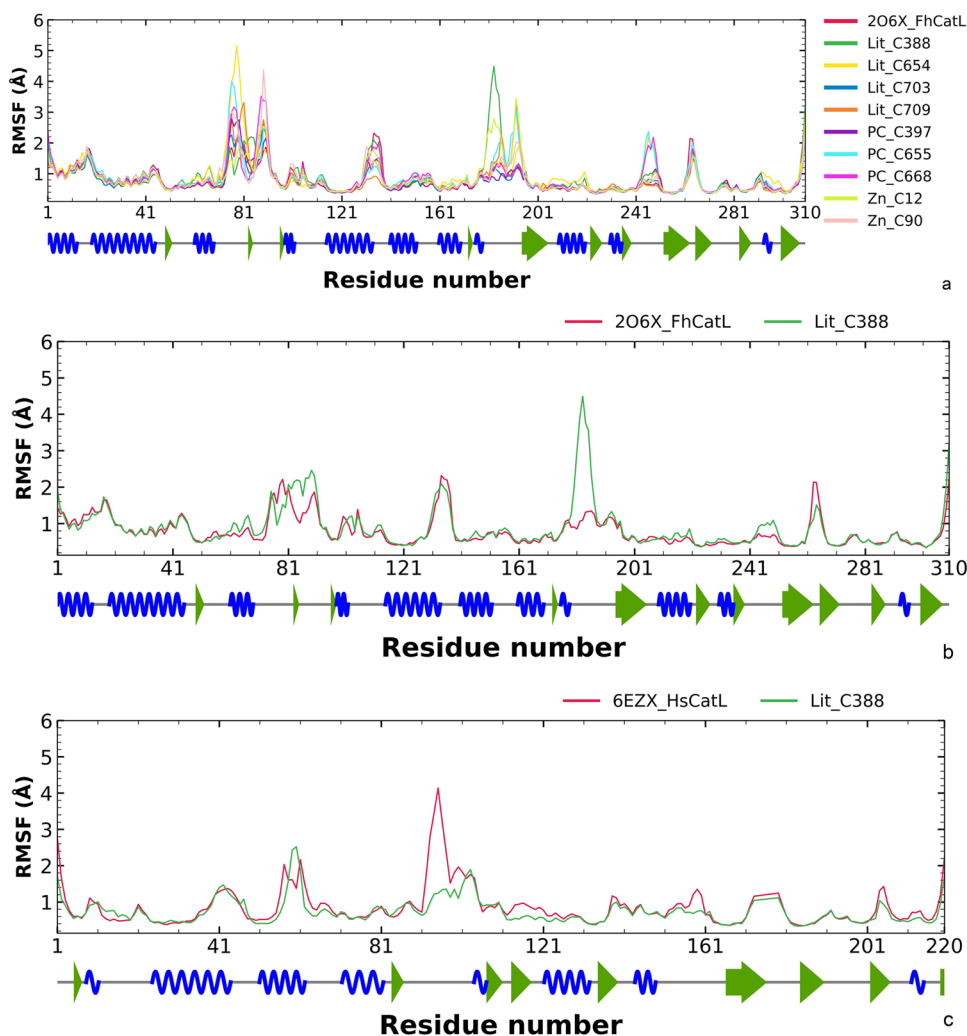
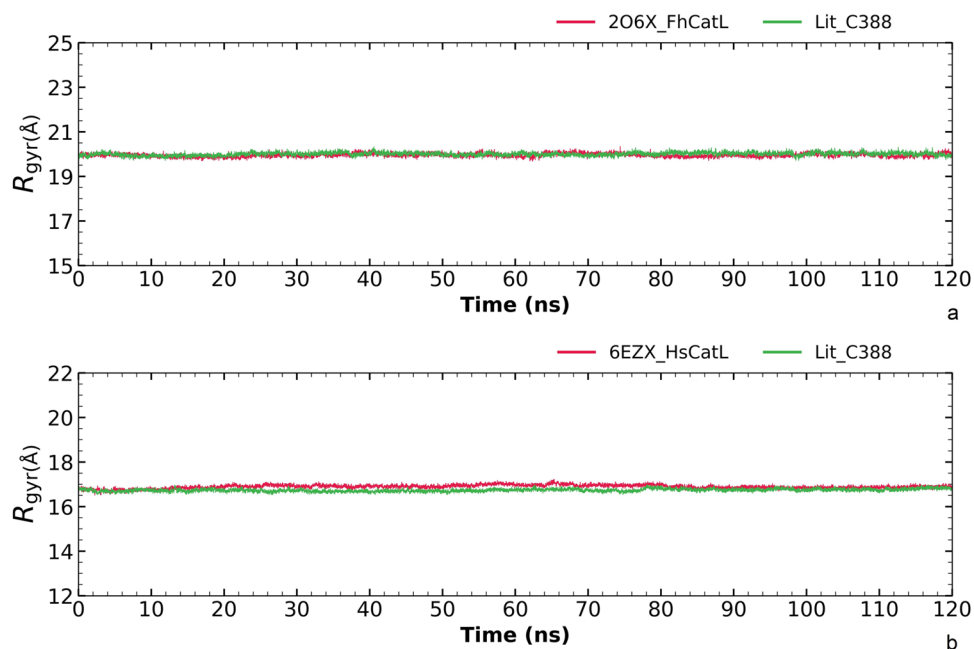


Fig. 23 Graphs for the radius of gyration for Lit_C388-*FhCatL* and Lit_C388-*HsCatL* complexes in comparison to receptors alone



Contact analysis of trajectory

The residue interaction frequency and the ligand-residue interaction mapping observed for the last third of the dynamics' trajectory with *FhCatL/HsCatL* for Lit_C388 are presented in Fig. 24.

Interaction analysis provides a clearer picture as to where the ligand moved toward to complement the RMSD analysis. As it may be observed in Fig. 24, the

most common interactions for Lit_C388 fail to occur with residues near the known catalytic dyad Cys25-His163 (*HsCatL*) and Cys116-His253 (*FhCatL*). In the case of *FhCatL* residues, Gln242, Ser243, and Gln244 are near His253 but point away from the catalytic dyad. A similar situation occurs for residues Ser157 and Ser158 in *HsCatL* which are near catalytic residue His163 but point away from the catalytic dyad. In this case, Lit_C388 does

Fig. 24 Interaction frequencies and ligand-residue interaction map for MD simulations of *FhCatL/HsCatL* complexes

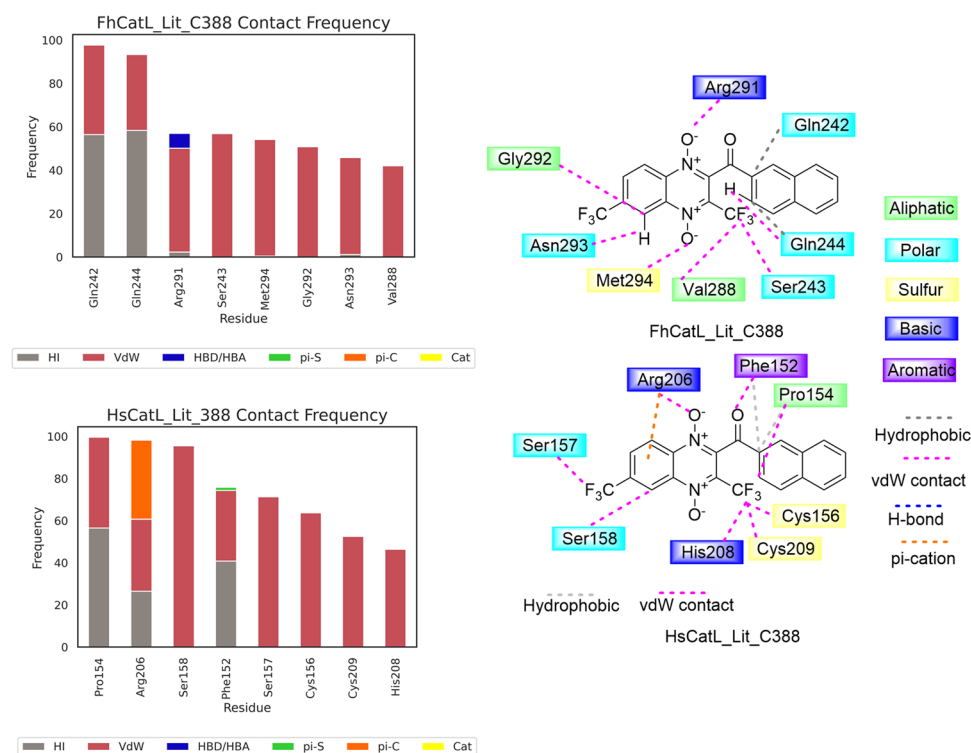


Fig. 25 Per-residue energy contribution for *Fh*CatL and *Hs*CatL complexes

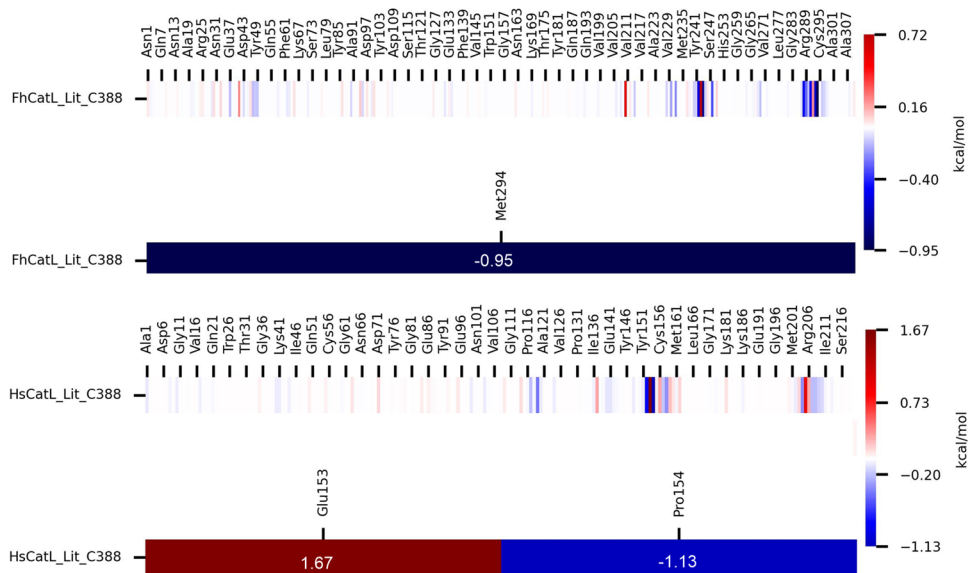


Table 4 Binding energy components for *Fh*CatL and *Hs*CatL complexes with Lit_C388 in kcal/mol

	ΔE_{elec}	ΔE_{vdW}	ΔG_{polar}	$\Delta G_{nonpolar}$	$\Delta G_{binding}$
<i>Fh</i> CatL_Lit_C388	-1.72 ± 0.12	-33.16 ± 0.25	19.68 ± 0.28	-3.26 ± 0.02	-18.46 ± 0.23
<i>Hs</i> CatL_Lit_C388	-0.53 ± 0.18	-34.8 ± 0.19	22.01 ± 0.32	-2.94 ± 0.02	-16.26 ± 0.34

not show a high potential to behave as inhibitors of either protein, parasite, or human. The hydrogen bond count for *Fh*CatL and *Hs*CatL is 0.089 and 0.01 hydrogen bonds per frame, respectively, which suggests low binding stability potential. Still, there exists a proximity between the predicted pose and the catalytic dyad, and there are antecedents of this type of compounds behaving as cathepsin L inhibitors may be worth continuing to explore their inhibitory potential (Fig. 25).

MMPBSA

The $\Delta G_{binding}$ as calculated by MMPBSA as presented in Table 4 shows that Lit_C388 binds with more affinity toward *Fh*CatL over *Hs*CatL. Though its inhibitory potential is low, this calculated binding energy suggests that if inhibition occurs a preference toward parasite over human may be expected. A single residue with an attractive contribution beyond -0.9 kcal/mol was calculated for Lit_C388 when bound to *Fh*CatL, which occurs with Met294, a residue pointing toward the catalytic dyad but about 9 Å away from His253. In the case of the binding with *Hs*CatL, two residues overcame the 0.9 kcal/mol threshold one with a repulsive contribution, Glu153, and one with an attractive contribution Pro154, both of which point away from the catalytic dyad, still suggesting a higher potential for Lit_C388 toward *Fh*CatL.

Conclusions

In this study, a series of 1851 QNO derivatives obtained from different chemical libraries were analyzed against three parasite targets *Tc*TR, *Tv*TIM, and *Fh*CatL and their human homologs *Hs*GR, *Hs*TIM and *Hs*CatL.

For *Tc*TR/*Hs*GR analysis, both top scored QNO derivatives Lit_C777 and Zn_C38 show a high potential to behave as *Tc*TR inhibitors. The interactions profile obtained from the molecular dynamics' trajectory for both tested ligands are similar for parasite and human proteins. Still, they show a preference for *Tc*TR over *Hs*GR as per MMPBSA binding energy calculation and higher hydrogen bond count for parasite protein over human protein and both ligands having attractive energy contributions with residues near the catalytic triad.

For *Tv*TIM/*Hs*TIM analysis, Lit_C208 showed the highest potential to inhibit *Tv*TIM selectively, as it holds an interaction pattern, obtained from the molecular dynamics' trajectory, that includes His94, a residue from the catalytic dyad, while it interacts away from the catalytic dyad in *Hs*TIM. Similarly, as per MMPBSA calculation, it possesses a higher binding affinity toward parasite over the human protein, and the residues that provide attractive contribution point toward the catalytic dyad of *Tv*TIM, whereas an opposite behavior is seen for *Hs*TIM. Conversely, Zn_C76 showed a potential

to inhibit *Hs*TIM, as per its interaction profile which includes Lys13, a residue from the catalytic dyad, though as per MMPBSA per-residue energy contribution it shows this interaction to be a repulsive contribution.

It was possible to find through blind docking strategy of 20 randomly picked quinoxaline derivatives a docking site for QNO derivatives on the *Fh*CatL crystal, which was used for further docking studies.

For *Fh*CatL/*Hs*CatL analysis, Lit_C388 shows low potential to behave as an inhibitor, as it shows an interaction pattern, obtained from the molecular dynamics' trajectory, which does not hold any interactions near the catalytic dyad. As per MMPBSA residue contribution a single residue is about 9 Å away from catalytic dyad, and that is oriented toward the catalytic cavity provides an attractive energy contribution, Met294. On the other hand, the residues contributing in *Hs*CatL both point away from catalytic dyad.

Altogether, this study permitted going from a broad range of quinoxaline derivatives using in silico tools selects a concise set of potentially useful molecules that may behave as inhibitors of their intended targets, which can then be tested in vitro to corroborate this proposed activity.

Supplementary Information The online version contains supplementary material available at <https://doi.org/10.1007/s00894-023-05579-4>.

Author contribution All authors contributed to the study conception and design. Material preparation, data collection, and analysis were performed by Alonzo González-González, Domingo Méndez-Álvarez, and Lenci K. Vázquez-Jiménez, Timoteo Delgado-Maldonado, Eyra Ortiz-Pérez, Alma D. Paz-González, Debasish Bandyopadhyay, and Gildardo Rivera. The first draft of the manuscript was written by Alonzo Gonzalez-Gonzalez, and Gildardo Rivera, and all authors commented on previous versions of the manuscript. All authors read and approved the final manuscript.

Funding This work was supported by Secretaria de Investigacion y Posgrado del Instituto Politécnico Nacional (Grants 20220935 and 20230935).

Data availability The datasets generated during and/or analyzed during the current study are available in the supplementary material.

Declarations

Competing interests The authors declare no competing interests.

References

- Méndez-Álvarez D, Herrera-Mayorga V, Juárez-Saldivar A et al (2021) Ligand-based virtual screening, molecular docking, and molecular dynamics of eugenol analogs as potential acetylcholinesterase inhibitors with biological activity against *Spodoptera frugiperda*. *Mol Divers*. <https://doi.org/10.1007/S11030-021-10312-5>
- Juárez-Saldivar A, Schroeder M, Salentin S et al (2020) Computational drug repositioning for Chagas disease using protein-ligand interaction profiling. *Int. J. Mol. Sci.* 21:1–16. <https://doi.org/10.3390/IJMS21124270>
- Ferraro F, Merlino A, Gil J, Cathepsin L et al (2019) inhibitors with activity against the liver fluke identified from a focus library of quinoxaline 1,4-di-N-oxide derivatives. *Molecules*. 24(2348 24):2348. <https://doi.org/10.3390/MOLECULES24132348>
- Villalobos-Rocha JC, Sánchez-Torres L, Nogueada-Torres B et al (2014) Anti-Trypanosoma cruzi and anti-leishmanial activity by quinoxaline-7-carboxylate 1,4-di-N-oxide derivatives. *Parasitol. Res.* 113:2027–2035. <https://doi.org/10.1007/s00436-014-3850-8>
- Chacón-Vargas KF, Nogueada-Torres B, Sánchez-Torres LE et al (2017) Trypanocidal activity of quinoxaline 1,4 Di-N-oxide derivatives as trypanothione reductase inhibitors. *Molecules*. 22:220. <https://doi.org/10.3390/molecules22020220>
- Carta A, Loriga M, Paglietti G et al (2004) Synthesis, anti-mycobacterial, anti-trichomonas and anti-candida in vitro activities of 2-substituted-6,7-difluoro-3-methylquinoxaline 1,4-dioxides. *Eur. J. Med. Chem.* 39:195–203. <https://doi.org/10.1016/J.EJMECH.2003.11.008>
- Rivera N, Rojas M, Zepeda A et al (2013) In vivo genotoxicity and cytotoxicity assessment of a novel quinoxalinone with trichomonad activity. *J. Appl. Toxicol.* 33:1493–1499. <https://doi.org/10.1002/JAT.2819>
- Estevez Y, Quiliano M, Burguete A et al (2011) Trypanocidal properties, structure–activity relationship and computational studies of quinoxaline 1,4-di-N-oxide derivatives. *Exp. Parasitol.* 127:745–751. <https://doi.org/10.1016/j.exppara.2011.01.009>
- Machado-Silva A, Cerqueira PG, Grazielle-Silva V et al (2016) How Trypanosoma cruzi deals with oxidative stress: antioxidant defence and DNA repair pathways. *Mutat. Res. Rev. Mutat. Res.* 767:8–22. <https://doi.org/10.1016/j.mrrev.2015.12.003>
- Palos I, Moo-Puc R, Vique-Sánchez JL et al (2021) Esters of quinoxaline-7-carboxylate-1,4-di-N-oxide as Trichomonas vaginalis triosephosphate isomerase inhibitors. *Acta. Pharm.* 71:485–495. <https://doi.org/10.2478/ACPH-2021-0032>
- Benítez-Cardoza CG, Brieba LG, Arroyo R, et al (2021) Triosephosphate isomerase as a therapeutic target against trichomoniasis. *Molecular and Biochemical Parasitology* 246. <https://doi.org/10.1016/j.molbiopara.2021.111413>
- Vique-Sánchez JL, Caro-Gómez LA, Brieba LG, Benítez-Cardoza CG (2020) Developing a new drug against trichomoniasis, new inhibitory compounds of the protein triosephosphate isomerase. *Parasitol. Int.* 76:102086. <https://doi.org/10.1016/J.PARINT.2020.102086>
- Vázquez-Jiménez LK, Moreno-Herrera A, Juárez-Saldivar A, et al (2021) Recent advances in the development of triose phosphate isomerase inhibitors as antiprotozoal agents. *Curr Med Chem* 28. <https://doi.org/10.2174/0929867328666210913090928>
- Ferraro F, Merlino A, dell'Oca N, et al (2016) Identification of chalcones as Fasciola hepatica cathepsin L inhibitors using a comprehensive experimental and computational approach. *PLoS Negl Trop Dis* 10. <https://doi.org/10.1371/JOURNAL.PNTD.0004834>
- Wijffels GL, Panaccio M, Salvatore L et al (1994) The secreted cathepsin L-like proteinases of the trematode, Fasciola hepatica, contain 3-hydroxyproline residues. *Biochem J* 299:781. <https://doi.org/10.1042/BJ2990781>
- Petersen EF, Goddard TD, Huang CC et al (2004) UCSF chimera—a visualization system for exploratory research and analysis. *J Comput Chem* 25:1605–1612. <https://doi.org/10.1002/JCC.20084>
- O'boyle NM, Banck M, James CA, et al (2011) Open Babel: an open chemical toolbox. <https://doi.org/10.1186/1758-2946-3-33>
- Forli S, Huey R, Pique ME et al (2016) (2016) Computational protein–ligand docking and virtual drug screening with the AutoDock

- suite. *Nat. Protoc.* 11(5 11):905–919. <https://doi.org/10.1038/nprot.2016.051>
19. Trott O, Olson AJ (2010) AutoDock Vina: Improving the speed and accuracy of docking with a new scoring function, efficient optimization, and multithreading. *J. Comput. Chem.* 31:455–461. <https://doi.org/10.1002/jcc.21334>
 20. Alvarez G, Martínez J, Aguirre-López B et al (2014) New chemotypes as *Trypanosoma cruzi* triosephosphate isomerase inhibitors: a deeper insight into the mechanism of inhibition. *J. Enzyme. Inhibition. Med. Chem.* 29:198–204. <https://doi.org/10.3109/14756366.2013.765415>
 21. Álvarez G, Aguirre-López B, Varela J et al (2010) Massive screening yields novel and selective *Trypanosoma cruzi* triosephosphate isomerase dimer-interface-irreversible inhibitors with anti-trypanosomal activity. *Eur. J. Med. Chem.* 45:5767–5772. <https://doi.org/10.1016/j.ejmech.2010.09.034>
 22. Adasme MF, Linnemann KL, Bolz SN et al (2021) PLIP 2021: expanding the scope of the protein–ligand interaction profiler to DNA and RNA. *Nucleic. Acids. Res.* 49:W530–W534. <https://doi.org/10.1093/NAR/GKAB294>
 23. Abraham MJ, Murtola T, Schulz R et al (2015) GROMACS: high performance molecular simulations through multi-level parallelism from laptops to supercomputers. *SoftwareX* 1–2:19–25. <https://doi.org/10.1016/j.softx.2015.06.001>
 24. Duan Y, Wu C, Chowdhury S, Lee MC, Xiong G, Zhang W, Yang R, Cieplak P, Luo R, Lee T et al (2003) A point-charge force field for molecular mechanics simulations of proteins based on condensed-phase quantum mechanical calculations. *J. Comput. Chem.* 24:1999–2012. <https://doi.org/10.1002/jcc.10349>
 25. Wang J, Wang W, Kollman PA, Case DA (2006) Automatic atom type and bond type perception in molecular mechanical calculations. *J. Mol. Graph. Model.* 25:247–260. <https://doi.org/10.1016/j.jmgm.2005.12.005>
 26. Wang J, Wolf RM, Caldwell JW, Kollman PA, Case DA (2004) Development and testing of a general amber force field. *J. Comput. Chem.* 25:1157–1174. <https://doi.org/10.1002/jcc.20035>
 27. Jorgensen WL, Chandrasekhar J, Madura JD, Impey RW, Klein ML (1983) Comparison of simple potential functions for simulating liquid water. *J. Chem. Phys.* 79:926–935. <https://doi.org/10.1063/1.445869>
 28. Bussi G, Donadio D, Parrinello M (2007) Canonical sampling through velocity rescaling. *J. Chem. Phys.* 126:014101. <https://doi.org/10.1063/1.2408420>
 29. Berendsen HJC, Postma JPM, van Gunsteren WF, DiNola A, Haak JR (1984) Molecular dynamics with coupling to an external bath. *J. Chem. Phys.* 81:3684–3690. <https://doi.org/10.1063/1.448118>
 30. Parrinello M, Rahman A (1981) Polymorphic transitions in single crystals: a new molecular dynamics method. *J. Appl. Phys.* 52:7182–7190. <https://doi.org/10.1063/1.328693>
 31. Polishchuk P, Kutlushina A, Bashirova D et al (2019) Virtual screening using pharmacophore models retrieved from molecular dynamic simulations. *Int J Mol Sci* 20(5834 20):5834. <https://doi.org/10.3390/IJMS20235834>
 32. Lemkul JA (2019) From proteins to perturbed Hamiltonians a suite of tutorials for the GROMACS-2018 Molecular Simulation Package [Article v1.0]. *Living. J. Comput. Mol. Sci.* 1:5068–5068. <https://doi.org/10.33011/LIVECOMS.1.1.5068>
 33. Darden T, York D, Pedersen L (1993) Particle Mesh Ewald: An $N \cdot \log(N)$ Method for Ewald sums in large systems. *J. Chem. Phys.* 98:10089–10092. <https://doi.org/10.1063/1.464397>
 34. Hess B, Bekker H, Berendsen HJC, Fraaije JGEM (1997) LINCS: a linear constraint solver for molecular simulations. *J. Comput. Chem.* 18:1463–1472. [https://doi.org/10.1002/\(SICI\)1096-987X\(199709\)18:12%3c1463::AID-JCC4%3e3.0.CO;2-H](https://doi.org/10.1002/(SICI)1096-987X(199709)18:12%3c1463::AID-JCC4%3e3.0.CO;2-H)
 35. Bouysset C, Fiorucci S (2021) ProLIF: a library to encode molecular interactions as fingerprints. *J. Cheminform.* 13:72. <https://doi.org/10.1186/s13321-021-00548-6>
 36. Kumari R, Kumar R, Lynn A (2014) g_mmpbsa —a GROMACS tool for high-throughput MM-PBSA calculations. *J. Chem. Inf. Model.* 54:1951–1962. <https://doi.org/10.1021/ci500020m>
 37. Baker NA, Sept D, Joseph S et al (2001) Electrostatics of nanosystems: application to microtubules and the ribosome. *Proc. Natl. Acad. Sci. USA.* 98:10037–10041. <https://doi.org/10.1073/pnas.181342398>
 38. Salentin S, Haupt VJ, Daminelli S, Schroeder M (2014) Polypharmacology rescored: protein–ligand interaction profiles for remote binding site similarity assessment. *Prog. Biophys. Mol. Biol.* 116:174–186. <https://doi.org/10.1016/j.pbiomolbio.2014.05.006>
 39. Torres E, Moreno-Viguri E, Galiano S et al (2013) Novel quinoxaline 1,4-di-N-oxide derivatives as new potential antichagasic agents. *Eur. J. Med. Chem.* 66:324–334. <https://doi.org/10.1016/j.ejmech.2013.04.065>
 40. Chang TC, Park JH, Colquhoun AN et al (2018) Evaluating the catalytic importance of a conserved Glu97 residue in triosephosphate isomerase. *Biochem. Biophys. Res. Commun.* 505:492–497. <https://doi.org/10.1016/j.bbrc.2018.09.076>
- Publisher's note** Springer Nature remains neutral with regard to jurisdictional claims in published maps and institutional affiliations.
- Springer Nature or its licensor (e.g. a society or other partner) holds exclusive rights to this article under a publishing agreement with the author(s) or other rightsholder(s); author self-archiving of the accepted manuscript version of this article is solely governed by the terms of such publishing agreement and applicable law.